AFRL-AFOSR-VA-TR-2024-0204

Characterizing In-situ matrix properties of polymer composites using Digital Volume Correlation (DVC) and modeling; Static and fatigue loading

Anthony Waas
REGENTS OF THE UNIVERSITY OF MICHIGAN
1109 GEDDES AVE, SUITE 3300
ANN ARBOR, MI, 48109
USA

04/11/2024
Final Technical Report

Air Force Research Laboratory
Air Force Office of Scientific Research
Arlington, Virginia 22203
Air Force Materiel Command

REPORT DOCUMENTATION PAGE

PLEASE DO NOT RETURN YOUR FORM TO THE ABOVE ORGANIZATION.

1. REPORT DATE	2. REPORT TYPE	3. DATES COVERED	
20240411	Final	START DATE 20191215	END DATE 20231214

4. TITLE AND SUBTITLE
Characterizing In-situ matrix properties of polymer composites using Digital Volume Correlation (DVC) and modeling; Static and fatigue loading

5a. CONTRACT NUMBER	5b. GRANT NUMBER	5c. PROGRAM ELEMENT NUMBER
	FA9550-20-1-0014	61102F
5d. PROJECT NUMBER	**5e. TASK NUMBER**	**5f. WORK UNIT NUMBER**

6. AUTHOR(S)
Anthony Waas

7. PERFORMING ORGANIZATION NAME(S) AND ADDRESS(ES)
REGENTS OF THE UNIVERSITY OF MICHIGAN
1109 GEDDES AVE, SUITE 3300
ANN ARBOR, MI 48109
USA

8. PERFORMING ORGANIZATION REPORT NUMBER

9. SPONSORING/MONITORING AGENCY NAME(S) AND ADDRESS(ES)	10. SPONSOR/MONITOR'S ACRONYM(S)	11. SPONSOR/MONITOR'S REPORT NUMBER(S)
Air Force Office of Scientific Research 875 N. Randolph St. Room 3112 Arlington, VA 22203	AFRL/AFOSR RTA1	AFRL-AFOSR-VA-TR-2024-0204

12. DISTRIBUTION/AVAILABILITY STATEMENT
A Distribution Unlimited: PB Public Release

13. SUPPLEMENTARY NOTES

14. ABSTRACT
In this project, the matrix properties and the fatigue response of fiber reinforced laminated composites is experimentally investigated with a view to developing a physics based numerical model. Different length scales at which damage accumulates is examined. At the fiber/matrix scale digital volume correlation is adopted in an in-situ microCT facility to measure internal 3D strains associated with the onset of splitting in zero fiber plies, (fiber/matrix cracking parallel to the fibers) and matrix cracking in the orthogonal 90 degree plies. Furthermore, these measurements, taken for a notched composite show the sequence of damage mechanisms - delamination first, followed by splitting or vice-versa. At the laminate scale, these mechanisms are seen to manifest in a similar manner. An IR camera is used for the laminate scale tests to measure the evolving temperature fields in fatigue loading and also as a clear indicator of the local temperature rise associated with matrix cracks. The results clearly capture the failure mechanisms, the 3D strain fields of importance, the temperature fields and the failure loads all of which aid in the verification and validation of a physics based numerical model.

15. SUBJECT TERMS

16. SECURITY CLASSIFICATION OF:			17. LIMITATION OF ABSTRACT	18. NUMBER OF PAGES
a. REPORT	b. ABSTRACT	c. THIS PAGE		
U	U	U	UU	53

19a. NAME OF RESPONSIBLE PERSON	19b. PHONE NUMBER *(Include area code)*
GREGG ABATE	

Standard Form 298 (Rev.5/2020)
Prescribed by ANSI Std. Z39.18

Award Information

Title: Characterizing In-situ matrix properties of polymer composites using Digital Volume Correlation (DVC) and modeling; Static and fatigue loading
Sponsor Award Number: FA9550-20-1-0014
Period of Performance: 12/15/2019-12/14/2023
Award Total: $505,316
Award Type: Grant

Journal Papers

1. Rojas-Sanchez, F., & Waas, A. M., 2023 (Currently under review). Characterization of damage initiation in fiber reinforced composites from high resolution experimental data. Composites Part A.
2. Rojas-Sanchez, F., & Waas, A. M., 2023. Microscale experimental results and their implications for mesoscale modeling of damage initiation in cross-ply fiber reinforced composites. Composites Part B: Engineering, 257, 110663.

Conference Papers

1. Rojas Sanchez, J. F., & Waas, A. M., 2023. High Resolution Experimental Study of Damage Initiation in Cross-Ply Laminate Using Digital Volume Correlation. In ASME SSDM 2023
2. Rojas Sanchez, J. F., & Waas, A. M., 2023. Characterization of meso-scale progressive failure model for fiber reinforced composites from high resolution experimental data. In AIAA SCITECH 2023 Forum (CP 2023-0591).
3. Rojas Sanchez, J. F., & Waas, A. M., 2022. High resolution imaging of fatigue damage evolution in fiber reinforced composites using digital volume correlation for model validation. In AIAA SciTech 2022 Forum (CP 2022-0669).

Honors and Awards:

2023 Rackham International Research Award
2023 Rackham Graduate Student Research Grant

Grant Participants

Fernando Rojas, Anthony M. Waas, Paul Davidson, Jose
Jose Vicente Calvo

Partners/Collaborators

Jose Vicente Calvo (visiting student, from Spain)
Wooseok Ji (Ulsan National Institute of Science and Technology - UNIST, Korea)

Patents - None

Inventions - None

Licenses - None

Technologies

New data related to fatigue damage growth using fast scan microCT equipment used at UNIST, Korea (worlds fastest microCT capability)

Development of the principal discipline(s) of the project

The main result of the project is a detailed understanding of the damage initiation mechanisms in notched cross-ply laminated structures subjected to monotonic and fatigue tension loading, and their influence on final failure. This understanding was gained by collecting a sequence of synchrotron Computed Tomography (CT) scans from 3 sets of experiments and conducting high resolution Digital Volume Correlation (DVC) analyses. In the first experiment, a specimen was loaded incrementally to failure in relatively large steps (10 steps in total), and an in-situ CT scan was collected at each step. This experiment revealed the global damage sequence that these structures undergo before final failure and provided an estimate of the load at which damage initiation begins. In the second experiment, the damage initiation mechanisms were studied in detail. A specimen was loaded in small increments around the previously identified point of damage initiation and a CT scan was collected at each increment. This experiment revealed the order in which damage initiation mechanisms begin. The latter finding is critical for characterization of material properties via inverse modeling as different material properties lead to different damage initiation sequences. Last, in a 3rd experiment, 3 specimens were loaded cyclically off-situ for different number of cycles (5,50, and 500), up to the load of damage initiation, and then a CT scan of each was taken. This experiment revealed the damage propagation caused by fatigue loading and allowed to compare it against that obtained from monotonic loading.

In combination, the results from the 3 previously described sets of experiments are expected to have an important impact on our knowledge of how composites fail by challenging underlaying assumptions in commonly-used failure theories and modeling techniques. This project achieves this goal by bridging the gap between the high resolution results that modern modeling techniques can offer and the relatively low resolution results that are commonly collected from experiments. By gathering high resolution DVC data from these experiments, it is possible to make thorough accuracy assessments of the intricacies of modern composite failure modeling techniques, to correct wrong assumptions, and to better characterize material properties via inverse modeling. Moreover, the experimental results obtained will also grow our fundamental knowledge of fatigue in composites, which is still an active field of research and relevant to multiple aerospace engineering applications among other fields.

Other disciplines:

Describe the impact in this reporting period on the development of human resources

Nothing to report

Describe the impact on teaching and educational experiences

Nothing to report

Describe the impact in this reporting period on physical, institutional, and information resources that form infrastructure

Nothing to report

Impact on society beyond science and technology

Nothing to report

Table of Contents

Chapter 1 – Review of fatigue models

Fatigue of a composite structure is a damage mechanism caused by repeated loading at levels below its ultimate quasi-static limit. Fatigue is detrimental to the stiffness and strength of the material, and it is particularly severe at locations with stress concentrations such as cut outs. This damage mechanism is driven by progressive nucleation, propagation, and coupling of matrix cracks and delamination zones. Depending on the laminate and loading, fatigue can also lead to fiber breakage. A diagram of the typical fatigue process in composites is shown in Figure 1.

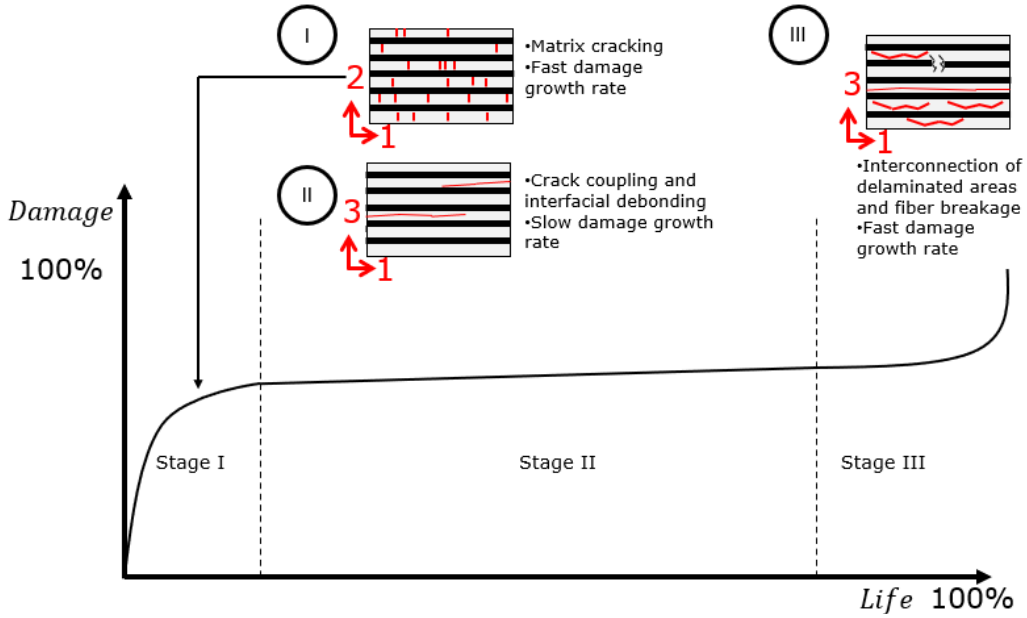

Figure 1Damage stages in the fatigue of composites

It is challenging to model fatigue of composites efficiently because it is a multiscale phenomenon in time and space. At certain points of the fatigue life, a matrix crack can propagate significantly within a single cycle. At other points, microcracks can take long periods of time to couple and form a macroscopic crack. Modeling the development of individual cracks cycle by cycle would be impossible, therefore, models in the literature use different levels of simplifications to propose an approach that is computationally manageable.

The simplest approach to model different modes of microdamage in composites is called Continuum Damage Mechanics (CDM). This method consists of modeling the composite as a uniform orthotropic material and degrading its elastic properties and strengths as the material fatigues to account for the effective result of the development of cracks and delamination zones. A diagram that illustrates the concept of CDM is shown in Figure 2.

Van Paepegem et al. [1] proposed a CDM fatigue model for plain-woven glass/epoxy composites under uniaxial displacement-controlled fatigue loading. In their model, they implemented a cycle jumping scheme. This scheme consists of simulating explicitly only selected cycles in the fatigue life of the structure and skipping the ones in between. After each simulation, the rate of damage growth is assessed according to an experimentally characterized fatigue law and used to determine an appropriate jump by which a certain level of damage growth has been reached. The process is

repeated until a given global stopping criterion is reached. A diagram that illustrates the cycle jumping scheme is shown in Figure 3.

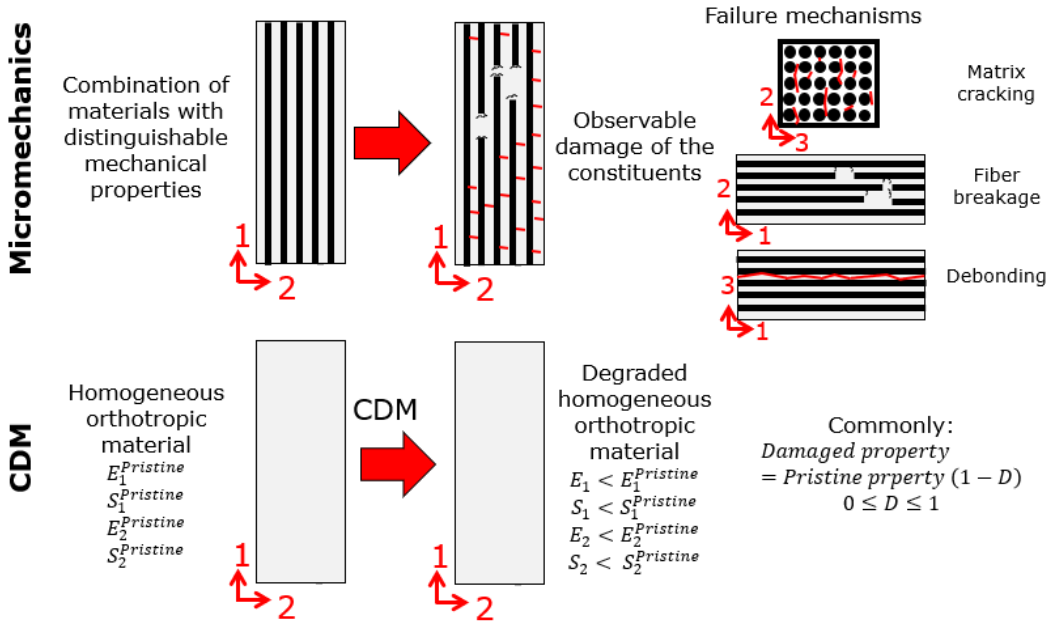

Figure 2 Implementation of continuum damage mechanics

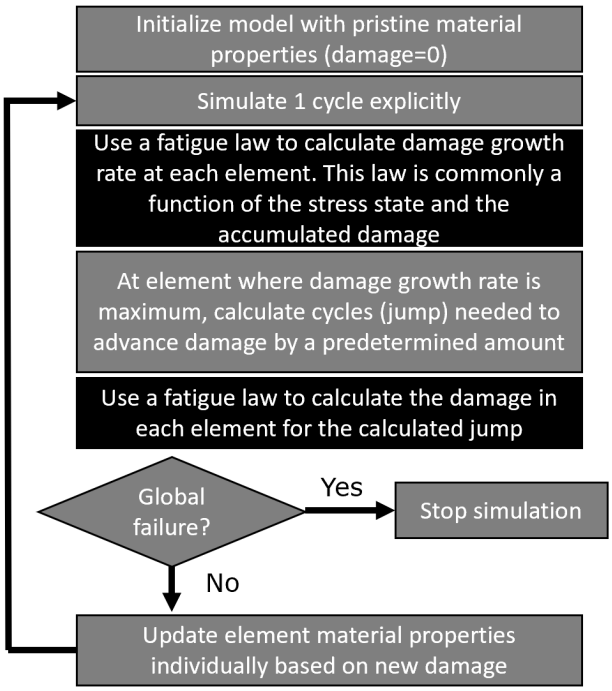

Figure 3 Cycle jumping scheme

In their model, Van Paepegem et al. only considered a 1-dimensional problem of a specimen under cyclic bending, they used 5 fitting constants in their fatigue law, and they determined their values via reverse engineering by fitting experimental force-cycle curves. Although the proposed model was

reported to have good correlation with experimental data, an independent dataset was not used for validation. Moreover, because of its oversimplified formulation, the model has a limited scope of application. The model cannot capture delamination, and it is not applicable to other stacking sequences, loadings, or specimen geometries.

NASA also developed a CDM fatigue model for composites called ADEAL [2]. ADEAL is a CDM transversely isotropic fatigue model developed as an extension of the NLCDR [3] model for isotropic metals. The adaptation from isotropic to transversely isotropic materials was done by introducing anisotropic damage surfaces. The model was developed originally for metal composites and later used for carbon/epoxy composites [4]. A single variable is used in the model to capture micro and macroscopic damage. The growth of this damage variable is driven by 3 significant invariants related to stress states predominant in damage modes. The first invariant is related to transverse normal stress and dictates matrix cracking. The second invariant is related to shear stress and dictates interfacial degradation. The third invariant is related to longitudinal normal stress and dictates fiber breakage. The reasoning behind why extending the NLCDR model for isotropic metals, which was thoroughly validated, to transversely isotropic metal composites is valid is because, in a sense, both materials have similar failure modes. Both materials start fatiguing due to failure mechanisms at the microstructural level. In the case of isotropic metals, mechanisms at this level include dislocations, cavities and slip bands. In composites, failure of the microstructure is related to matrix cracking. Then, in both materials, when cracks reach a size of approximately 1 mm, macroscopic propagation begins to occur. The failure mechanisms for both types of materials are illustrated in Figure 4.

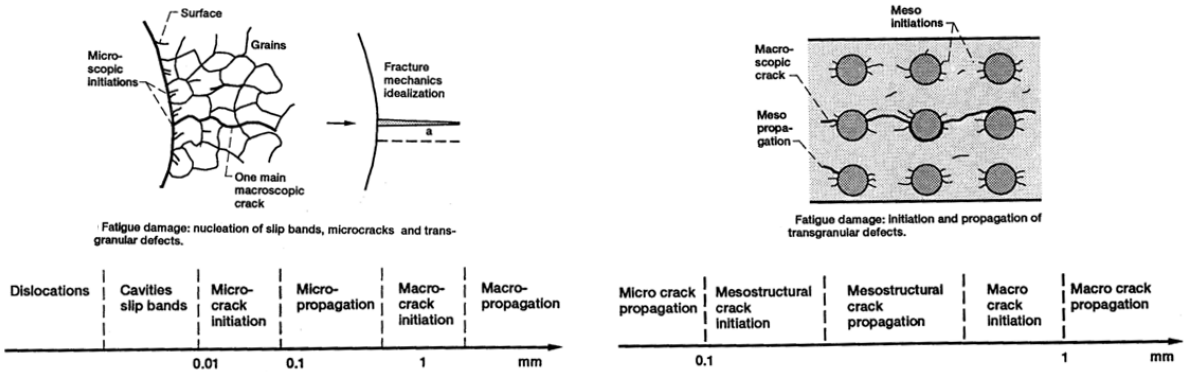

Figure 4 Comparison of failure modes between isotropic metals and transversely isotropic metal composites

One important difference between isotropic metals and fiber-reinforced composites is the damage evolution that the materials have throughout their lives [5], which wasn't explicitly accounted for when extending the NLCDR model to transversely isotropic composites. Fatigue damage progression in metals is commonly very slow at the beginning, but once damage has been initiated, it grows rapidly. On the other hand, damage in composites have a short period at the beginning of their lives where damage grows rapidly (stage 1), then the damage growth rate slows down for most of the composite's life (stage 2), and at the end it grows up very rapidly (stage 3). The difference between the damage evolution for each material is illustrated in Figure 5. Because of this legacy from metals in the formulation of the model, ADEAL has an important drawback, which is that it produces diffused-like damage patterns as opposed to sharp cracks propagating along the fibers, which would be more realistic for composites.

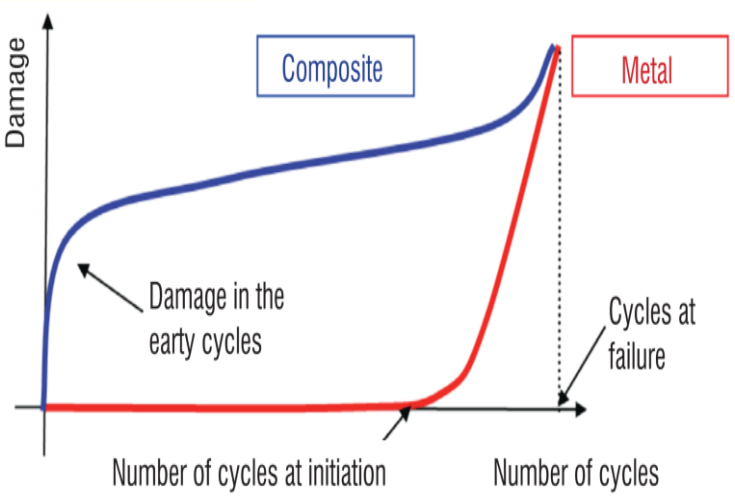

Figure 5 Difference of fatigue damage progression between isotropic metals and fiber-reinforced composites [5]

Shokrieh et al. [6, 7] also developed a CDM fatigue model for composites. Their main objective was to propose a methodology to predict the fatigue performance of a composite structure with an arbitrary stacking sequence and loading. Another point that Shokrieh et al. attempted to address was the characterization of material properties for the model using simple standardized tests. Fatigue tests have a large number of testing parameters (max stress, mean stress, loading direction, etc.), which makes it difficult to characterize the change in properties as a function of all these parameters. As a way to handle this challenge, Shokrieh et al. proposed to first conduct the tests illustrated in Figure 6 with a fixed set of parameters.

From these experimental results, Shokrieh et al. obtain fatigue life curves for the composite for different damage modes such as fiber tension, fiber compression, matrix tension, matrix compression, in-plane shear, and out-of-plane shear. The authors then implement a normalization method to enable the usage of the obtained fatigue curves with different loading parameters. Once an element in the model meets a given failure criterion, the element fails, and its stiffnesses and strengths are effectively set to 0. Although this method offers a convenient framework to model fatigue in composites, Shokrieh et al. did not provide a scientific explanation for why the idea of normalization is physically sound, they only provided a validation case study for which the idea was implemented and showed good correlation. This important assumption would have to be further investigated before it can be confidently used. Also, the method of setting the material stiffnesses and strengths to effectively 0 when a given failure mode is detected may not capture the correct propagation of damage and may show mesh dependence.

Type of test (Static or Fatigue)	Test Specimens	Standards	Notes
Fiber Tension	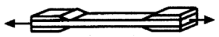	D 3039-76 D 3479-76	With Hydraulic Grips
Fiber Compression		———	With Hydraulic Grips
Matrix Tension		D 3039-76 D 3479-76	With Hydraulic Grips
Matrix Compression		D 3410-87	With Hydraulic Grips
In-Plane Shear	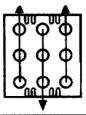	D 4255-83	Modified Notched Specimen
Out-of-Plane Shear		D 2733-70 D 2344-84	With Clamp

Figure 6 Characterization tests for fatigue model [7]

Chapter 2 – Microscale experimental results and their implications for mesoscale modeling of damage initiation

2.1 Introduction

Fiber-reinforced composites are increasingly being used in aerospace structural applications to meet several design requirements. These include fuel efficiency, flight performance, and durability. One challenge that commonly limits the extent to which the potential of these materials is exploited is the inability to model their deformation response accurately and efficiently including failure, which is necessary to deploy a design safely. Composites can be modeled at multiple length scales. If modeling is done at the microscale, accuracy could be high, but the macroscopic size of the structure that can be analyzed is very limited. On the other hand, if modeling is done at the macroscale to analyze a large structure by homogenizing all the plies in the composite as a uniform anisotropic material for instance, the fidelity is low. Modeling can also be done at any intermediate scale, which is commonly referred to as mesoscale.

To account for microstructural features of a composite and their effect on macroscopic performance, researchers have proposed different multiscale approaches. Broadly speaking, the two categories of approaches are concurrent and hierarchical. Concurrent models explicitly incorporate microscale features at every integration point. They offer high fidelity but at a great

computational cost. On the contrary, hierarchical models offer high computational speed by precomputing homogenized properties.

Faupel et al. [8] proposed a concurrent model for compression failure in UD composites. The model accounts for material properties and morphological features at several length scales such as fiber waviness to calculate the nucleation and propagation of compression kink bands. The results obtained using the model showed good correlation with theoretical calculations.

Su and Oskay [9] proposed a concurrent model using the Multiscale Discrete Damage Theory (MDDT) [10] for fatigue predictions of UD composites. In the proposed model, the microscale response is linked to the continuum representation of damage at the macroscopic scale based on averaging operations. Su and Oskay reported good correlation between the damage mechanisms predicted by their model and experimental observations.

Haj-Ali et al. [11] proposed a concurrent multiscale model for analysis of laminated composites subject to low-velocity impact. To overcome the high computational cost of concurrent models, Haj-Ali et al. used a parametric high fidelity generalized method of cells (PHFGMC) to train an Artificial Neural Network (ANN). They then used the ANN as a constitutive model to calculate the nonlinear and damage multiaxial behavior of the composite in the multiscale framework. Haj-Ali et al. reported close correlation with experimental results. Stuckner et al. [12] also proposed using a Machine Learning (ML) approach to accelerate the constitutive calculations in a concurrent multiscale model and reported a significant improvement in computational efficiency.

Christoff et al. [13] proposed a hierarchical approach to calculate the homogenized elastic properties of unidirectionally reinforced (UD) composites called the Asymptotic Homogenization Method (AHM). In AHM, a periodic unit cell is used to depict the nominal microstructure of the material and its effective properties are obtained through a variational formulation on a local boundary value problem [14]. Christoff et al. found a good correlation between the homogenized properties calculated using AHM and experimentally obtained values found in the literature.

Bhattacharyya and Adams proposed a hierarchical multiscale methodology to predict stiffness and strength of UD composite laminates. The method incorporates spatial distributions of micro-defects within a three dimensional Representative Unit Cell (RUC) and calculates the homogenized macroscopic properties using an eigenstrain-based multiscale modeling framework. Bhattacharyya and Adams reported that by characterizing the spatial distribution of defects in a composite and incorporating this information in their model, they were able to explain the wide variability in the stiffness and ultimate strength observed experimentally.

Another hierarchical multiscale methodology was introduced by Nguyen and Waas [15, 16, 17]. The method is referred to as the Semi-Discrete Damage Model (SD2M), and its main distinctive characteristic is that it proposes to account indirectly for microscale phenomena at the mesoscale in a computationally efficient ways. Microcracking is modeled using Schapery Theory [18]. Macroscopic cracking, delamination, and fiber damage are modeled using cohesive zone models. The method accounts for variations in the microstructure by assigning different strengths to the elements in the model according to a probability distribution. Close correlation of SD2M models with experimental results has been reported for tests such as open-hole tension and single-edge notched tension.

The need for a probabilistic determination of material properties in mesoscale models to account for variations in the microstructure has also been identified by other authors [19, 20]. However, whether only strengths or also elastic properties should be randomized and what is the best way to do it, is a discussion that is ongoing. Accounting for variations in effective elastic properties at the mesoscale level due to features in the microstructure of a composite like fiber volume fraction, void content, fiber packing, or fiber misalignment could lead to better estimations of the stress distribution in a structure. Consequently, more realistic predictions of crack formations in macroscopic Progressive Failure Analysis (PFA) models can be obtained.

To the best of the authors' knowledge, the influence that the mean through-ply-thickness fiber volume fraction has on the homogenized local elastic properties of a composite has not been investigated. This is particularly relevant because, typically, in mesoscale models, the elastic properties of a ply are assumed to be constant. These values are either calculated from a homogenization model, or measured experimentally. For computational efficiency, it is reasonable to vary the elastic properties due to different local fiber volume fractions along the in-plane direction, relegating the thickness direction variations to be secondary, as it is already being done for the strengths in the SD2M method. If the elastic properties were to be varied along the in-plane direction and assumed constant in the thickness direction, this would mean that there should be an observable experimental correlation between the local through-ply-thickness fiber volume fraction of a specimen, and the strain concentration intensity developed when loaded under a macroscopically uniform stress.

The purpose of the study presented in this chapter is to evaluate the need of accounting for local in-plane variations of elastic properties in mesoscale PFA models of composites due to fiber volume fraction inhomogeneities to achieve better predictions of crack formations. The problem of a rectangular cross-ply specimen loaded in tension is used as a case study to evaluate this need. The chapter is organized as follows. In section 1.2, experimental results in support of understanding the correlation between local fiber volume fraction and strain field inhomogeneities are reported. This is followed by a computational study in section 1.3 of the same problem studied experimentally in section 1.2, performed to support the experimental observations. Finally, concluding remarks that summarize the main findings are presented.

2.2 Experimental details and results

2.2.1 Global response of cross-ply specimens loaded in tension

In [21], Rojas and Waas report results on the experimentally characterization of rectangular cross-ply [90/0/90] specimens loaded axially in monotonic tension to failure to study the damage mechanisms of this laminate. During the test, they measured the strain field on one of the outer plies using Digital Image Correlation (DIC). In the measurements, they observed that before the formation of the transverse cracks that are typical in this type of laminate, significant strain field inhomogeneities were developed, even though axial strain is anticipated to be roughly uniform in the entire gage section at the scale at which measurements were taken. A summary of the results obtained in [21] are shown in Figure 7. It was hypothesized that a variation in local fiber volume fraction along the gage length of the specimen, caused the specimen to be locally more compliant in matrix-rich regions. If this were the case, it would suggest that in mesoscale models, it is important

to account for variations in elastic properties due to fiber volume fraction to correctly capture the local variations in the stress field, which consequently could significantly influence the location where cracks form. In this study, the strain inhomogeneities observed in the experimental results of [21] before crack formation are studied in detail in the context of assessing the need to account for variations in elastic properties in mesoscale PFA models for realistic crack formation predictions. Emphasis is put in comparing the strain inhomogeneities to the specimen's local fiber volume fraction because this is the microstructural feature that is expected to affect the elastic properties the most.

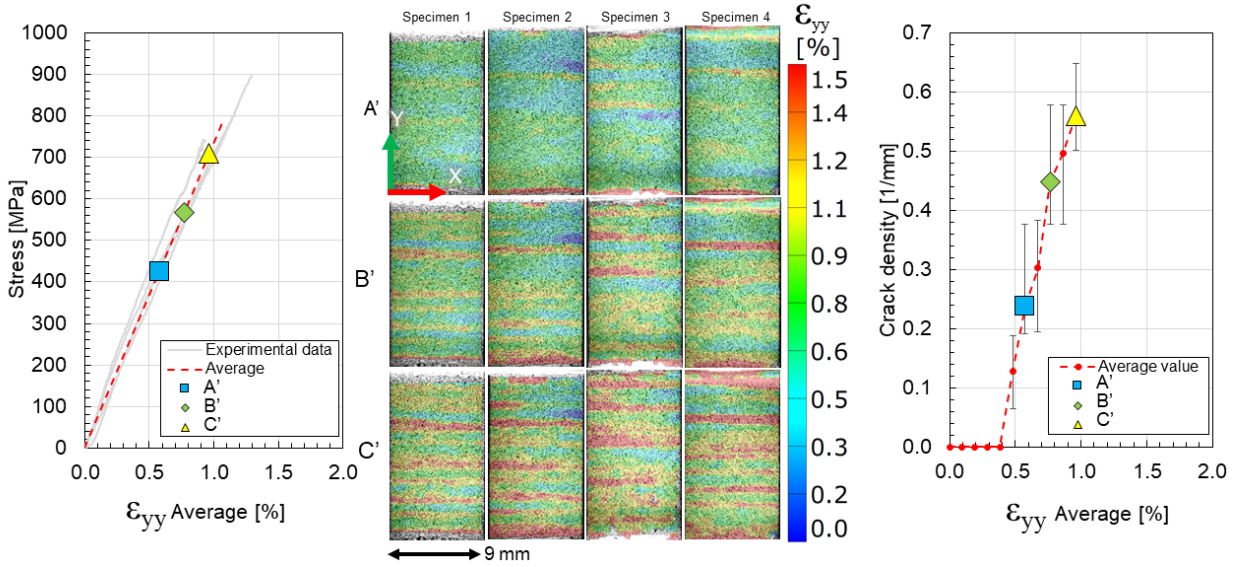

Figure 7 Stress-strain curve of unnotched specimens (left/top), crack density as function of axial strain (left/bottom)

2.2.2 Specimen characteristics

The material used to manufacture the specimens was a T800H/3631 prepreg system by Toray cured in a hot press. Rectangular specimens were cut from the cured panel using a waterjet cutter to a size of 45mm in length and 9mm in width. Then, fiberglass tabs were glued at the ends of the specimen using epoxy adhesive for a smooth load transfer from the grips to the specimen. The gage region length after gluing the tabs was 15 mm. Specimen geometry and dimensions are shown in Figure 8.

2.2.3 Determination of crack initiation point

The first step of the experimental procedure consisted of loading 4 specimens to failure. As the specimens were pulled axially in the y direction, the axial strain ε_{yy} was tracked at 10 points equally spaced along the specimen midline, as shown in Figure 8. A gap of 2mm between the edge of the fiberglass tabs and the immediate next measuring point was left at each end to avoid influencing the measurements by boundary condition effects. The average strain of all 10 measuring points was calculated at each frame in the DIC analysis and plotted against the average global strain, which was calculated by dividing the displacement between the upper and lower edges of the gage region (measured using DIC) and dividing it by the original gage region length.

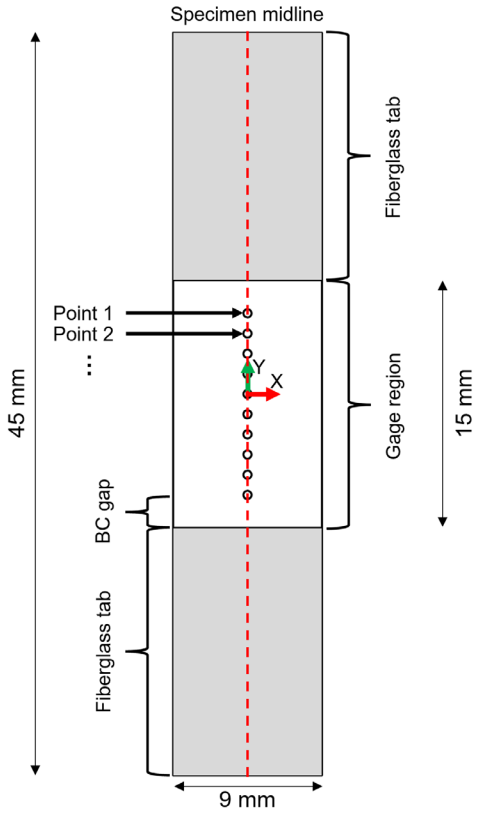

Figure 8 Specimen geometry and location of strain measuring points

When cracking initiates, the average strain of the 10 points diverges notoriously from a 1:1 ratio with the average global strain. This divergence point was identified for the 4 specimens and defined as the crack initiation point for future interrupted tests. The plots of the local versus global strain values of each specimen are shown in Figure 9. In this figure, the average strain of all 10 points, and a line with slope 1 are also plotted for clarity. The scatter in the strain profiles of each measurement point before crack formation is hypothesized to be due to through-thickness fiber volume fraction variations from one y coordinate to another. Testing this hypothesis is one of the main objectives of this chapter.

It can be observed from Figure 9 that the cracking initiation point ranges from 0.5% to 0.8% global strain. Therefore, to study the inhomogeneities in the strain field before cracking initiation, in the next experimental step, 3 pristine specimens were loaded to a 0.5% global strain and the test was interrupted. Similar plots to those in Figure 9 are shown in Figure 10 for these 3 new specimens along with a picture of the strain field at the point at which the test was interrupted. It can be observed that in all 3 cases, there was some cracking already initiated at 0.5% global strain, so the point at which the strain field was compared to the fiber volume fraction measurements of the specimen in the next experimental step was changed to be at 0.4% global strain. After the tests were interrupted, the specimens were unloaded and unmounted from the tensile station for microscopy inspection. More details are provided in section 1.2.4.

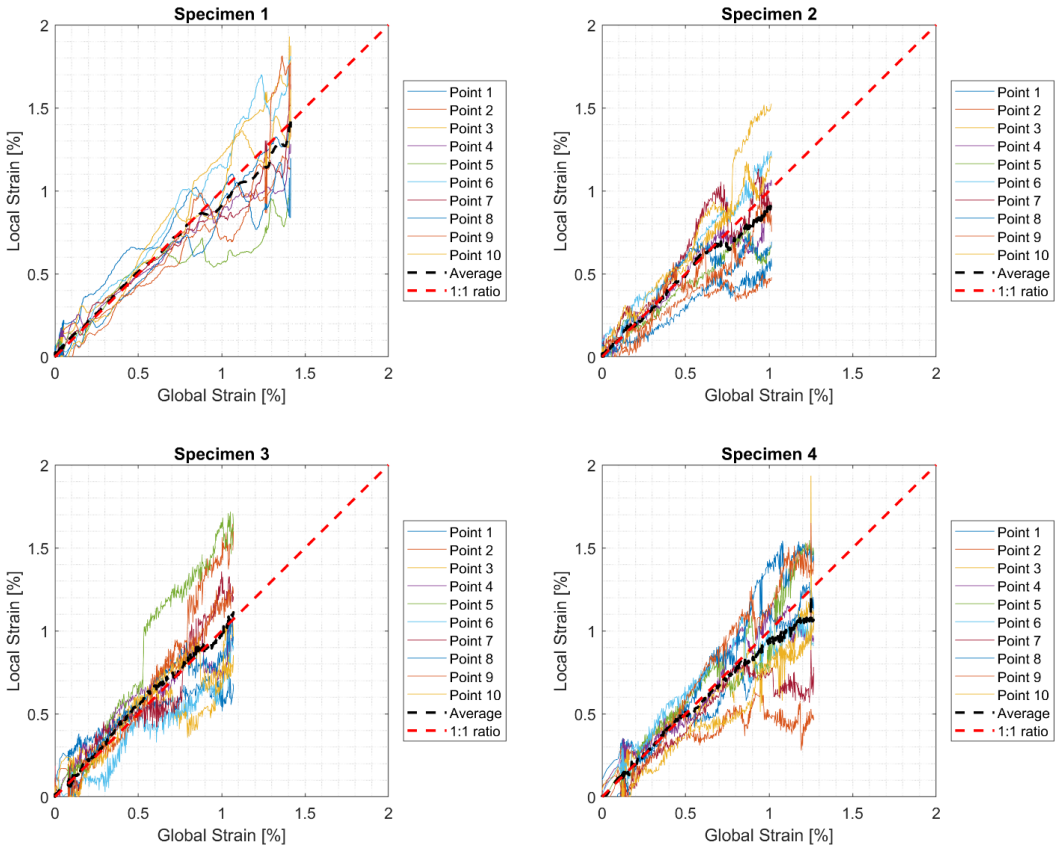

Figure 9 Local vs global strain measurements to determine crack initiation point

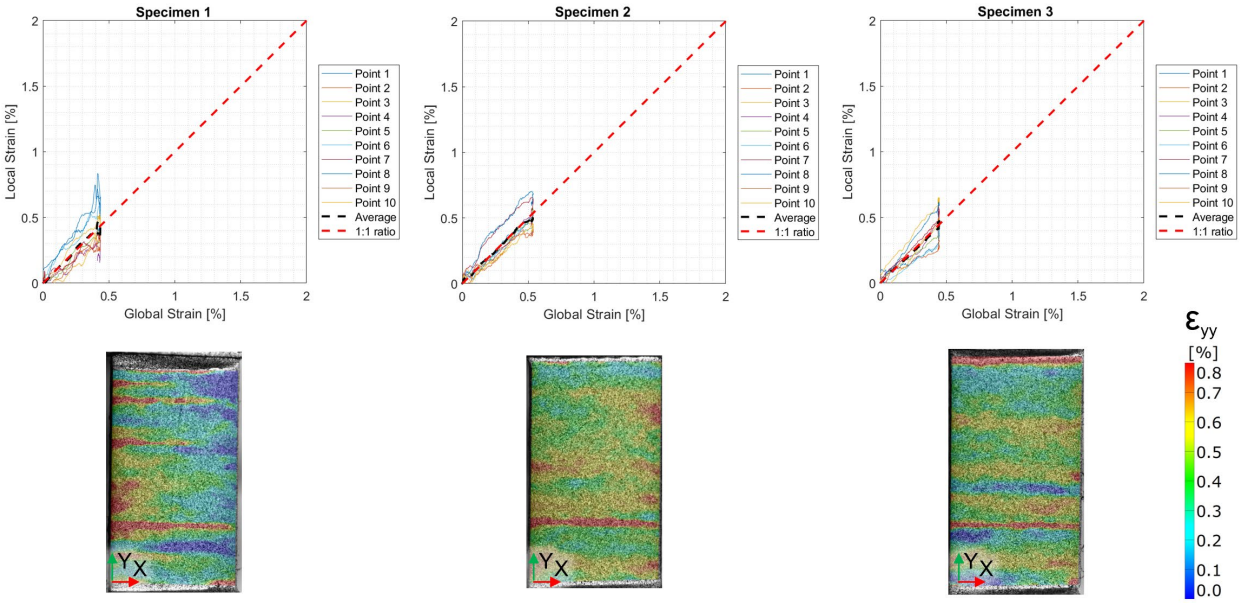

Figure 10 Results of specimens loaded to 0.5% global strain to study inhomogeneities in strain field

2.2.4 Experimental fiber volume fraction measurements

The 3 specimens that were loaded up to 0.5% global axial strain, were then unmounted from the tensile station, embedded in epoxy for microscopy inspection, and polished from one of the sides (yz plane) until reaching the midline of the specimen (Figure 8). Detailed microscopy images were taken of the entire gage length such that the individual fibers could be clearly resolved. A sample image of a portion of the cross section is shown in Figure 11. At this point, ideally, an automated image processing algorithm should be used to identify the ply contour, locate the center of each fiber, and measure their diameter to calculate analytically the fiber volume fraction of the specimen gage region from a digitized version of the microscopy image. The authors attempted to pursue this approach, however, they could not achieve satisfactory results that worked reliably for the entire gage length of the specimen, thus, an alternative procedure was followed.

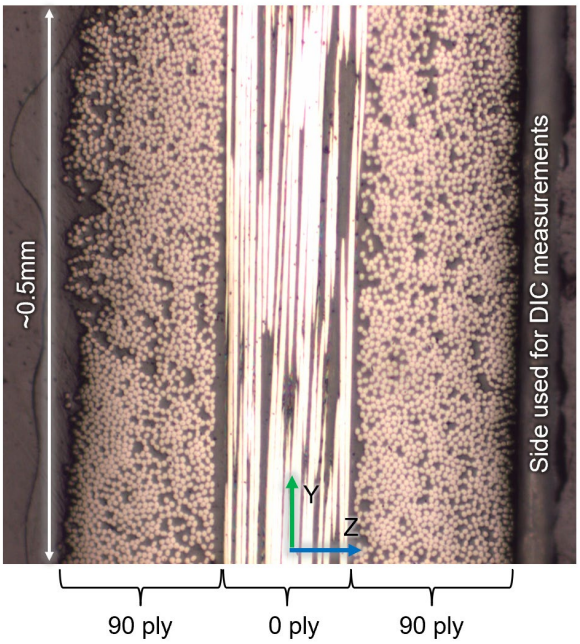

Figure 11 Sample microscopy image of specimen cross section

The alternative procedure consisted of selecting 10 small (~0.3mm) equally spaced sections along the gage length of one of the 3 specimens, and digitizing the sections by manually identifying the ply contour, locating the center of each fiber, and measuring their diameter. Then, using the digitized version of each of the sections, the fiber area fraction was calculated, which, assuming negligible fiber misalignment, is the same as the through-width fiber volume fraction of the ply at that y coordinate, therefore the terms fiber area fraction and fiber volume fraction will be used interchangeably for the rest of the chapter. The digitization process is illustrated in Figure 12. The average fiber volume fraction obtained for the 10 sections inspected was 0.40. Then, the contour of the entire gage length of the 3 specimens was manually digitized, and a binary classifier for each specimen was tuned to detect fiber and matrix pixels within the digitized contour such that the average fiber area fraction of the entire gage length matched the value previously found (0.40).

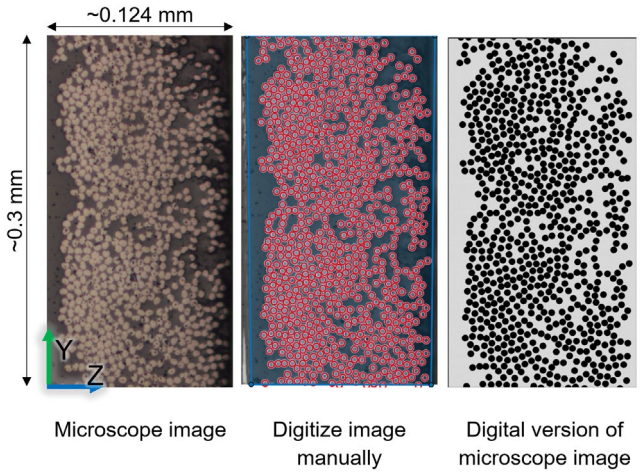

Figure 12 Digitization procedure for detailed fiber volume fraction measurements

In Figure 13, the original microscope image of a section of a specimen's gage region is shown as well as that same image with the binary classifier showing the pixels detected as fibers and those detected as matrix. Upon inspection, it can be observed that the classifier does a satisfactory job for approximately 2/3 of the ply thickness, except for the outer edge (right hand side), therefore, the classifiers were used to calculate the fiber volume fraction of the outer plies on which DIC measurements were taken. The poor performance of the classifier for regions near the surface is caused mainly by the irregularity of the specimen at these locations. When digitizing the contour of the specimens manually, it would be impractical to delimit accurately all the irregularities of the surface, therefore, some empty regions that are neither matrix nor fibers are mistakenly classified as matrix. This limitation of the experimental technique is addressed in the Finite Element (FE) models presented in section 1.3.

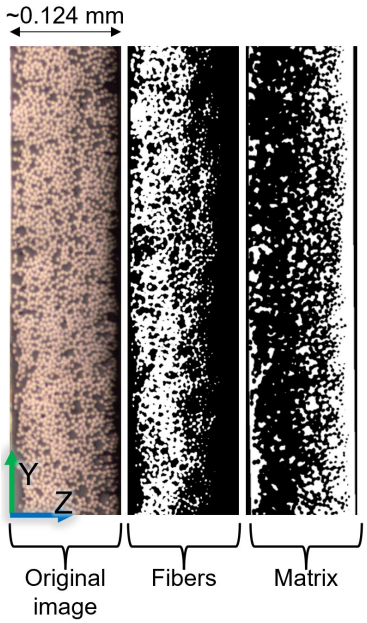

Figure 13 Sample of binary classifier to measure fiber volume fraction. In each filtered image white pixels correspond to the constituent of interest

The fiber volume fraction at a given y coordinate was calculated by selecting an interrogation window centered at that location and dividing the pixels detected as fibers by the total number of pixels in the interrogation window. For clarity, a diagram illustrating the procedure previously described is provided in Figure 14.

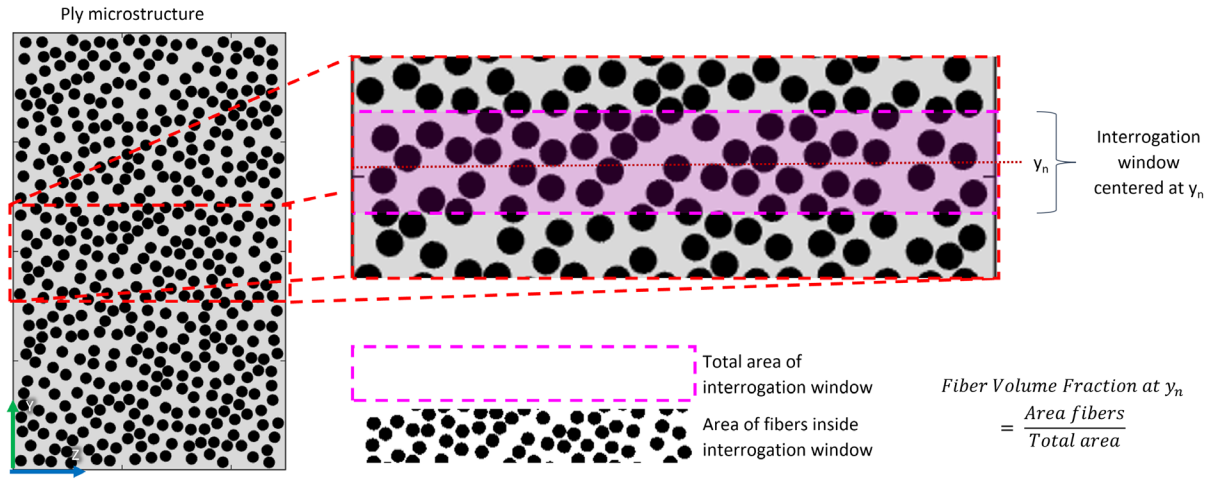

Figure 14 Calculation of Fiber Volume Fraction for a given interrogation window

The size of the interrogation window that was used was the same size as the facet used in the DIC analysis, which was 0.5mm long, so that they could be compared. In Figure 15, the comparison between fiber volume fraction and strain profiles (ε_{yy}) along the midline of the specimens tested are shown. In the figure, the 2 profiles of each specimen are plotted together so that they can be qualitatively compared. Also, matching fiber volume fraction and strain values, based on location, were plotted against each other to observe if there was any observable correlation between the two variables. A linear trendline was also drawn for the latter plot, and the correlation coefficient indicated in the plot title. By looking at the 3 correlation plots, it is clear that there is no trend between the through-ply-thickness fiber volume fraction and the strain (ε_{yy}) profiles.

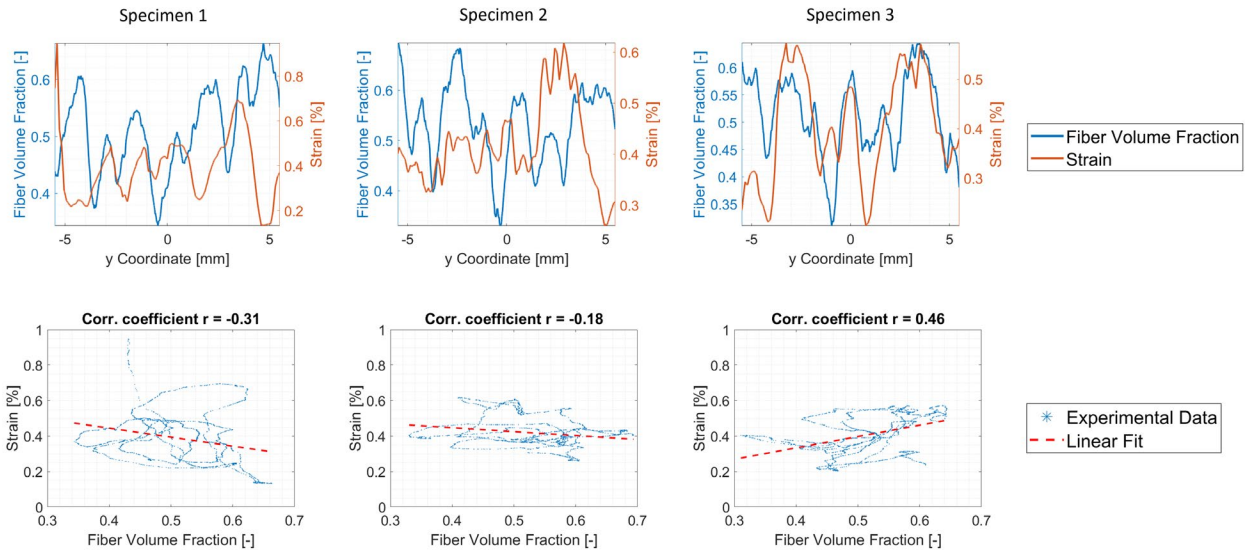

Figure 15 Comparison between fiber volume fraction and strain profiles from experimental measurements

2.3 Finite Element based results from micro models

To discard the possibility that the low correlation observed between fiber volume fraction and strain profiles in the experimental results was due to a poor measurement of the fiber volume fraction or an improper execution of the tensile tests, the same comparison was made from microscopic Finite Element simulation results. An overview of the models used is shown in Figure 16. In the interest of computational efficiency, the model was built using plane strain elements, and only a fraction of the gage region (along y) of the specimen was used. Due to symmetry, half of the thickness was modeled. Symmetry boundary conditions at the left-hand side of the 0 ply (z=0) were applied, displacement along y-direction was constrained at the bottom of the model (y=0), and a displacement was prescribed at the top (y=0.2mm) to reach a global axial strain value of 0.5%. The 0 ply was simulated using a homogenized orthotropic material model, and the 90 ply was modeled explicitly. The fiber size used in the 90 ply corresponded to the average fiber size measured from the microscope images as shown in Figure 12, which was equal to 5 microns. The fibers were placed using the Random Sequential Adsorption (RSA) algorithm [22]. Linear elastic material behavior was used for the matrix and the fibers, and geometric non-linearity was incorporated in the model for improved accuracy of the strain fields.

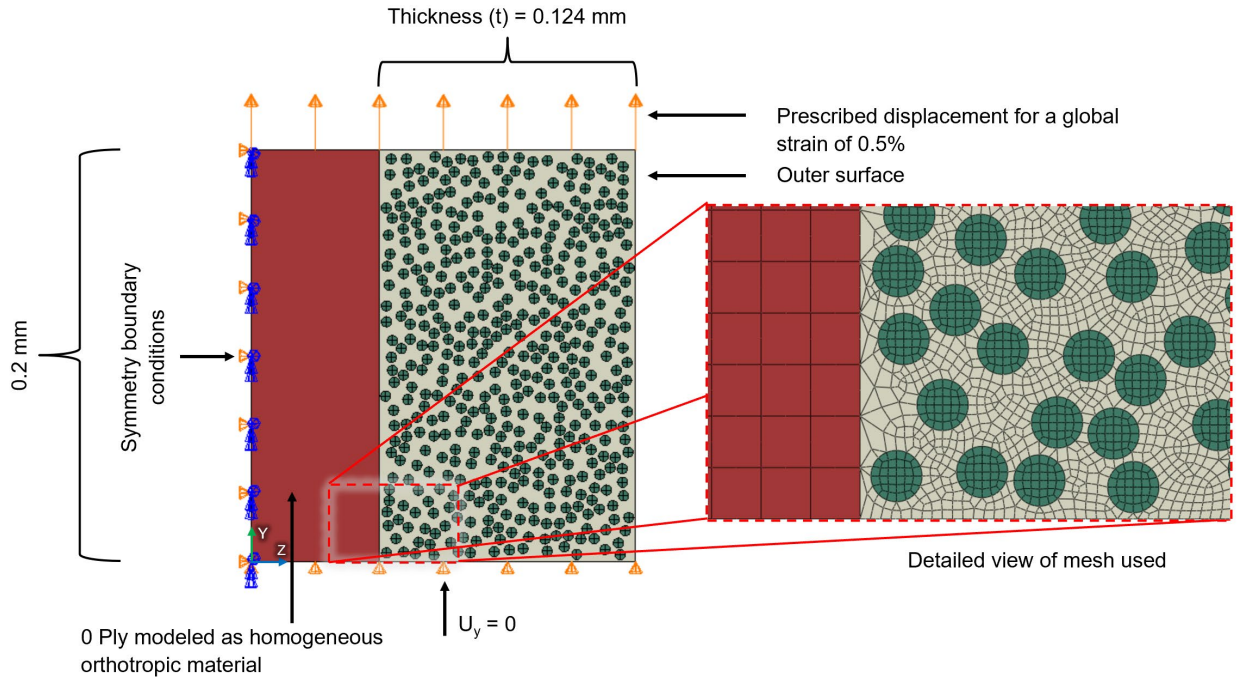

Figure 16 FE microscopic model

2.3.1 Validation of algorithm used for generation of artificial fiber patterns

To verify that the distributions artificially generated were equivalent to the ones observed in the specimens, first, the Ripley's K function [23] was calculated for the 10 manually digitized microscopic images discussed in the experimental section. The Ripley's K function is a useful tool to summarize and compare point patterns. Other more rigorous methods to compare statistical

equivalence between experimentally measured and artificially generated fiber patterns can be found in [24]. Additionally, “Micromechanics of composite materials” [25] is an excellent textbook that covers a wide variety of methods by which composite microstructures can be characterized accurately.

Ten artificial fiber patterns were generated using the RSA algorithm for boxes of the same nominal size as the experimental values, and the Ripley’s K function was calculated for these artificial patterns. A comparison between the Ripley’s K function for an r/D value of up to 15 between the experimental values and the ones from the artificial patterns is shown in Figure 17. It can be observed that although the results for the artificial patterns do not fully overlap with the experimental values, they are sufficiently close. The derivative g of the Ripley’s K function with respect to r was also calculated as an additional means of comparison. The point at which this derivative reaches an approximately constant value indicates the minimum RVE size of the pattern at which geometric homogeneity has been reached. The latter means that if a circle of this radius was drawn around a random fiber center in the pattern, no matter which fiber was picked, any circle would result in the same K value. A comparison between experimental values and those from artificial patterns is also shown in Figure 17. In this case, it can be observed that the values for the artificial patterns overlap completely with the experimental values, indicating once again that it is reasonable to assume that the RSA algorithm generates patterns that are statistically similar to those observed in the specimens experimentally.

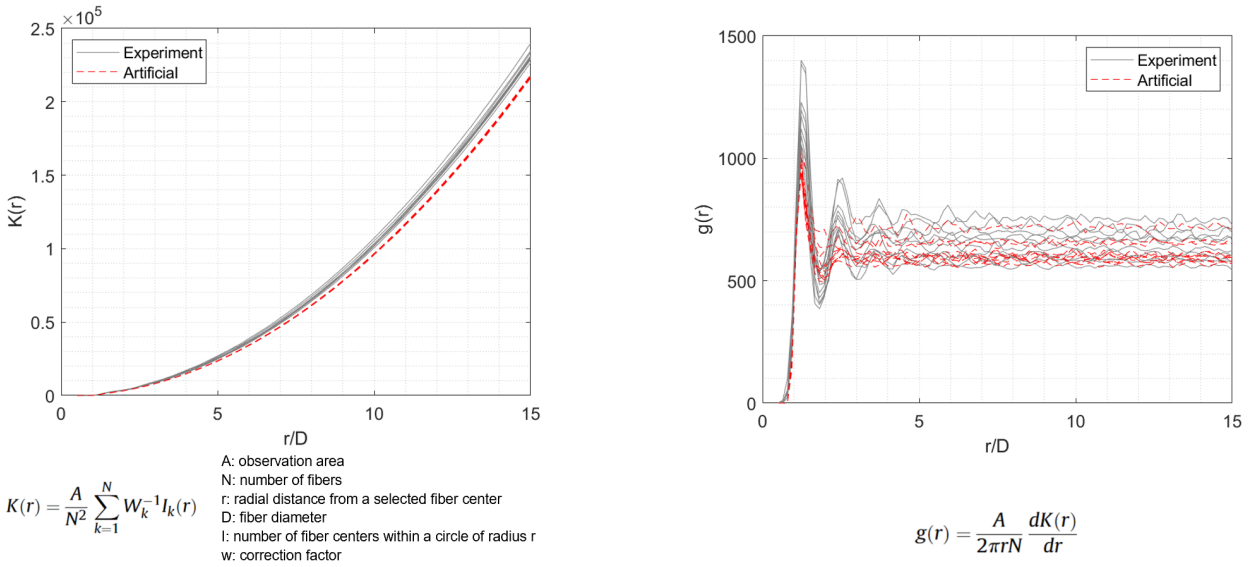

Figure 17 Comparison between experimentally measured and artificially generated fiber patterns using Ripley's K function and its derivative

2.3.2 Acquisition of constituent properties

To determine the properties of the matrix and the fibers, first, the matrix was assumed to have an isotropic material behavior and the fiber was assumed to have a transversely isotropic material behavior. Then, from [26], the homogenized elastic properties of the T800H/3631 system at 0.45 fiber volume fraction were obtained. These properties are listed in Table 1. Using these properties, a

gradient-decent optimization algorithm in combination with a micromechanics analytical model was used to find the properties of the constituents that best matched these homogenized properties. The micromechanics model used was the Concentric Cylinder Model [27]. The obtained properties of the constituents are shown in Table 2. It must be mentioned that when running the optimization algorithm, the fiber volume fraction was also treated as a variable to be found since the value reported in [26] was observed to yield inconsistent results. The fiber volume fraction obtained using the optimization algorithm was 0.57.

Table 1 Elastic properties of homogenized T800H/3631 system at 0.45 fiber volume fraction

Property	Value
E_1	169 GPa
E_2	9.62 GPa
G_{12}	4.50 GPa
v_{12}	0.349
v_{23}	0.490

Table 2 Constituent properties of T800H/3631 system

Constituent	Property	Value
Fiber	E_1	294 GPa
	E_2	184.50 GPa
	G_{12}	130.54 GPa
	v_{12}	0.286
	v_{23}	0.349
Matrix	E	3.67 GPa
	v	0.442

To validate the properties obtained in Table 2, the CCM method was used to calculate the homogenized properties obtained using these constituent properties and the fiber volume fraction found via optimization and comparing them against the homogenized properties reported in [26]. Both sets of properties are shown in Table 3. It can be observed that the sets are very close to each other. Apart from v_{23}, all the properties are within 10% of the values reported in [26], therefore, the constituent properties obtained via optimization were considered acceptable and used in the model shown in Figure 16. It should be noted that although the error obtained using CCM for v_{23} is large, the value of 0.49 reported in [26] is too close to 0.5, which is the Poisson's ratio of a perfectly incompressible material. Typically, only rubbers have a Poisson's ratio so close to 0.5, therefore it is likely that v_{23} was not characterized correctly in [26]. Thus, the mismatch in v_{23} obtained with CCM is considered to be acceptable.

Table 3 Comparison of homogenized properties reported in [26] and the ones obtained using CCM

Property	Value reported in [26]	Value obtained using CCM	Error
E_1	169 GPa	169 GPa	0%
E_2	9.62 GPa	10.15 GPa	6%
G_{12}	4.50 GPa	4.50 GPa	0%
v_{12}	0.349	0.349	0%
v_{23}	0.490	0.238	51%

2.3.3 Correlation results

Using the material properties, and a sufficiently fine mesh corresponding to 1/15 the fiber diameter and the fiber placement algorithm presented in sections 1.3.1 and 1.3.2, 10 different microscopic models such as shown in Figure 16 were generated. It is to be noted that with this mesh size the computed results for the transversely isotropic elastic constants agreed to within 2-3% of the CCM model predictions. A displacement control load was applied to achieve a global axial strain (ε_{yy}) of 0.5%, and then the strain distribution on the outer surface of the specimen was computed and compared against the local fiber volume fraction distribution of the 90 ply. The interrogation window used to compare the fiber volume fraction and the strain profiles had to be reduced from the one used previously in the experiments because the model analyzed was significantly smaller than the specimen's gage region due to limitations in computational resources. In this case, to select an appropriate interrogation window size (IW), first the fiber volume fraction distribution and strain field distribution were compared for one of the microscopic models at 5 different interrogation window sizes. These sizes varied logarithmically from a size equal to the fiber diameter (5 μm) to a size ten times that. The results are shown in Figure 18. To mimic the way in which strain measurements are obtained experimentally, the strain profiles shown were obtained from the nodal values of the model on the outer surface, i.e. no averaging through the thickness of the ply was made. It can be observed that as the interrogation window becomes larger, both profiles tend to a straight horizontal line. The strain profile tends to converge to a constant value equal to the average global axial strain (0.5%) and the fiber volume fraction profile tends to converge to a constant value equal to the global average fiber volume fraction (0.4). Also, it can be observed from the scatter plots of strain vs fiber volume fraction that at none of the interrogation window sizes there is a clear trend or a strong correlation.

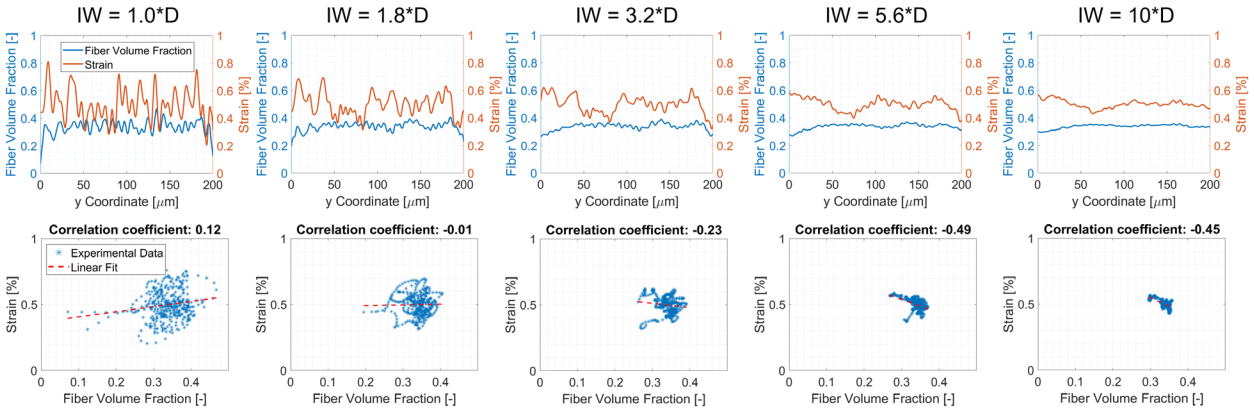

Figure 18 Comparison between fiber volume fraction and strain profiles from simulated data using different interrogation window sizes

Since an interrogation window size of 1.8 times the fiber diameter is a good balance between preserving the smallest features of the strain and fiber volume fraction profiles and showing global trends, that was the interrogation window size selected to analyze the results of the 10 different models that were created using the method illustrated in Figure 16. The results of these models are shown in Figure 19.

It is apparent that none of the 10 models show strong evidence of correlation between the fiber volume fraction and the strain profiles. The reason why there is not a correlation between the profiles becomes clear upon close inspection of the strain field. In Figure 20, the axial strain field results of one of the specimens is shown. This strain field is very similar to the field measured experimentally using DIC in [28]. In the figure, it can be observed that the variations in strain field at the outer surface are caused mainly by disturbances of the fibers closer to the surface and much less by any other factor at a larger scale.

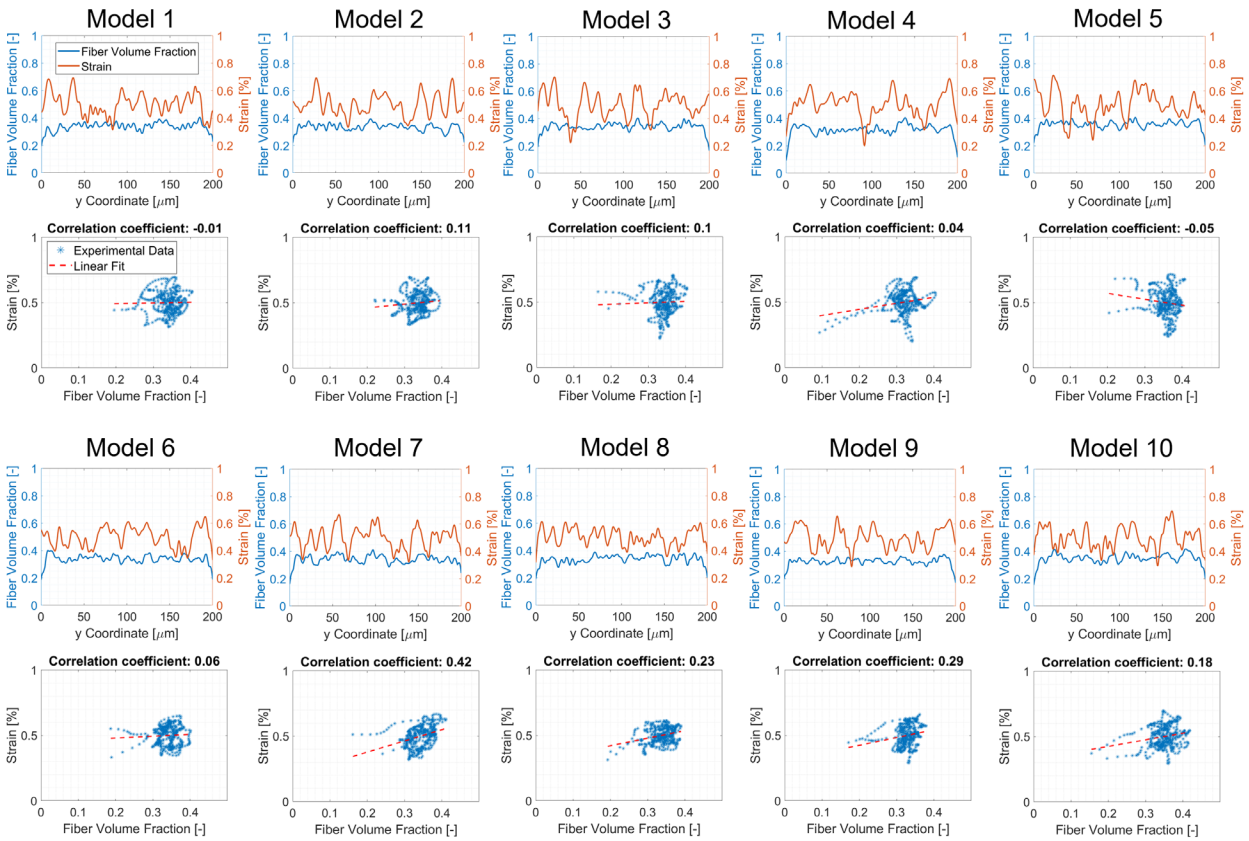

Figure 19 Comparison between fiber volume fraction and strain profiles from experimental measurements

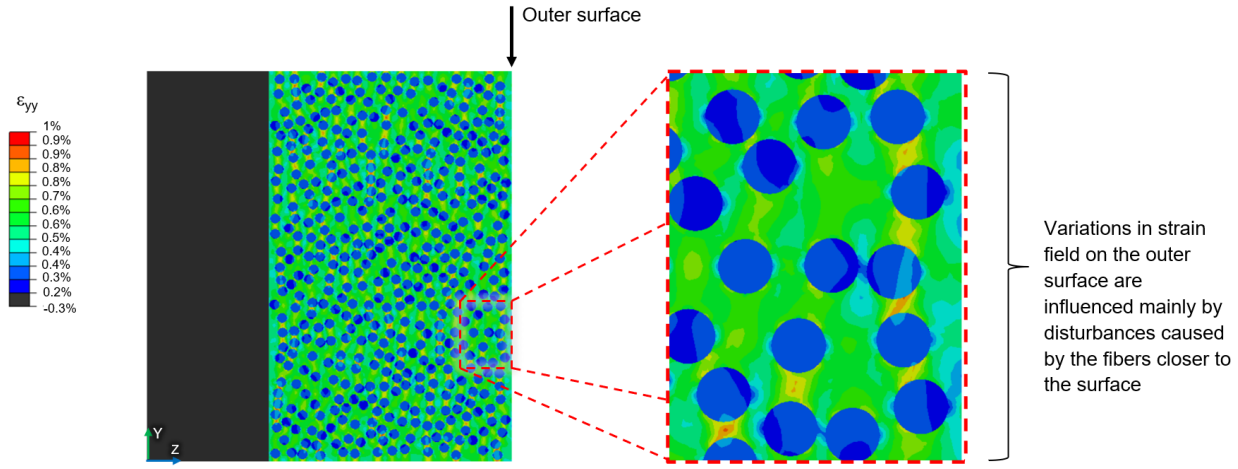

Figure 20 Sample strain field result

2.3.4 Determination of homogeneity threshold using RVEs

The observations made previously about the lack of correlation between through-ply-thickness fiber volume fraction and strain profiles for the case studied in this chapter suggest that in a mesoscale model, it is reasonable to use constant elastic properties throughout a ply and ignore the effects of fiber volume fraction variations. This observation has limitations mostly associated with the size of the element over which the properties are being homogenized relative to the point of scale separation for that particular material system. Doing a rigorous study to determine the limitations of this observation is beyond the scope of this chapter, however, a rough estimation of how large an element in a mesoscale model needs to be for this observation to be valid (at least for this material system) can be obtained by finding the homogeneity threshold. The homogeneity threshold is defined as the point at which an RVE displays the same homogenized elastic properties regardless of the specific microstructure distribution, for a given fiber volume fraction. This threshold marks the separation of scales in the composite from micro to mesoscale. Below this point, the homogenized properties are highly sensitive to variations in the microstructure distribution, but after it, the sensitivity decreases.

To find the homogeneity threshold for the material system used in this chapter, RVE of different sizes were constructed and the homogenized properties of each were calculated. Then, the homogenized properties were plotted against the RVE size, and the scatter for each size was observed. The RVE sizes that were used ranged from 3 to 20 times the fiber diameter. For each RVE size, 10 different microstructures were generated. Boxplots of the homogenized properties of each RVE size are shown in Figure 21. Red '+' markers in the boxplot indicate outliers as defined by Tukey's method. The homogenized properties obtained using the CCM micromechanical model are also indicated for reference since this method is considered to be of higher accuracy than the finite element models. It can be observed that the homogeneity threshold is approximately reached at a value of L/D (RVE length to fiber diameter ratio) equal to 15, because at this point, the scatter of each property is narrow and is close to the CCM solution. Therefore this is roughly the smallest size for which the observations from previous sections are valid. It is important to notice that the ply thickness has an L/D ratio approximately equal to 25. The latter suggests that small differences in the through-ply-thickness microstructural features at different y locations in the specimen do not have a significant

effect on the homogenized elastic properties of the composite. Since the L/D ratio at the homogeneity threshold is comparable to the ply thickness, this data suggests that one element through the thickness of each ply in a mesoscale model is sufficient to enforce separation of scale.

2.4 Conclusions

In this chapter, it has been shown that accounting for local in-plane variations of elastic properties due to local fiber volume fraction may not be the cause of variability in the local strain fields and thus is not the driving force for damage initiation. To achieve this, the correlation between through-ply-thickness fiber volume fraction and surface axial strain measurements in tensile tests of cross-ply [90/0/90] composite laminates was investigated. This problem was first studied experimentally, and then numerically using finite element models. In neither case, correlation between through-ply-thickness fiber volume fraction and surface axial strain was found. The finite element model results suggest that the strain variations on the surface of the outer 90 plies prior to crack formation are caused by local disturbances introduced by the fibers closest to the surface and not by the through-ply thickness fiber volume fraction. Therefore, it can be concluded that varying the elastic properties in a mesoscale model in the in-plane direction in an attempt to account for local fiber volume fraction inhomogeneities to improve the predictions of crack formation is not justified. On the contrary, homogeneous elastic properties throughout the model is a valid assumption.

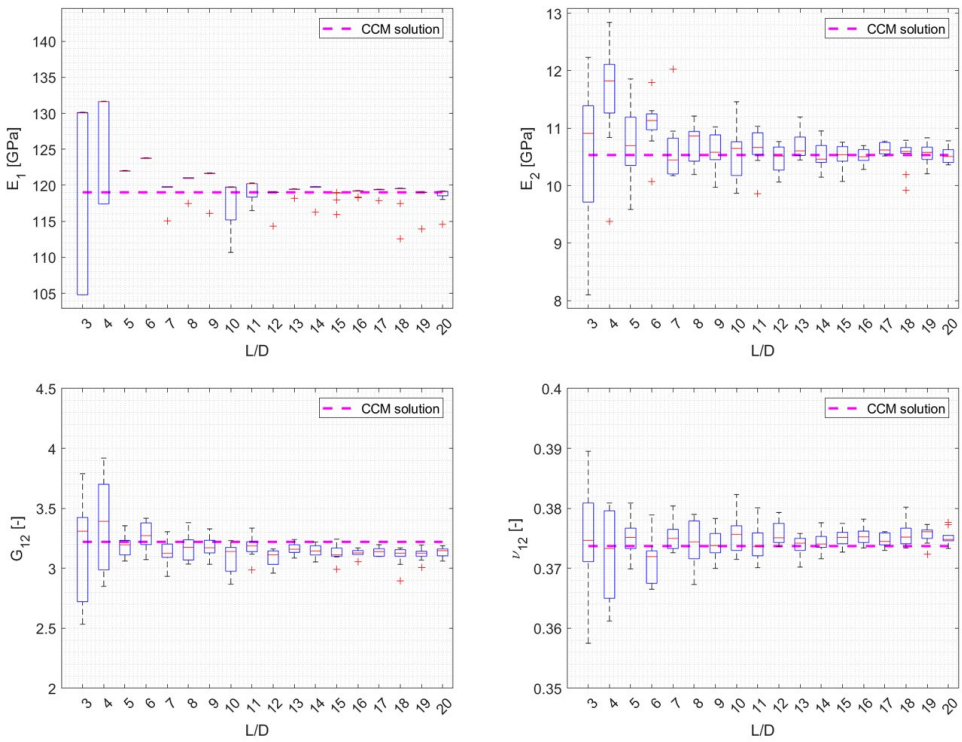

Figure 21 Fiber volume fractions and homogenized properties of RVEs with different sizes

Chapter 3 – Characterization of damage initiation from high resolution experimental data

3.1 Introduction

Carbon fiber reinforced composites (CFRC) offer advantages over traditional materials like metals in the design of lightweight structures with high mechanical performance. CFRC typically have higher strength-to-weight, and stiffness-to-weight ratios, better durability, and superior corrosion resistance. However, one challenge when designing with CFRC is to understand and accurately predict their failure mechanisms. The latter depend on the specific layup, microstructure architecture, properties of the constituents, stress concentrators in the structure such as cutouts, loading characteristics, and manufacturing method among other factors.

In order to design CFRC structures more efficiently by implementing approaches such as virtual development of allowables and certification by analysis, a robust methodology to accurately model the failure progression under different loading scenarios is required. This can lead to a reduction of expensive laboratory testing for the characterization of allowables and validation of aircraft designs. Such a methodology needs to be based on fundamental material properties and physics while also being practical and computationally efficient.

There is a large diversity of modeling methods in the literature that aim to achieve the goal previously described, some with a high level of sophistication, however, typically, it is difficult to assess thoroughly the accuracy of these models without experimental data that offers a similar level of detail. The collection of high resolution experimental data that provide insight into the damage mechanisms of CFRC at the mesoscale is invaluable for the verification of progressive failure analysis (PFA) models currently used for the design of aircraft, rockets, ships, and vehicles.

Unlike glass fiber reinforced composites [29, 30, 31], with CFRC it is impossible to observe internal damage using the backlight method because the material is opaque. Therefore, different alternative methods have been used to overcome this challenge for the collection of detailed experimental observations of damage. The most common methods are ultrasonic scanning [32, 33, 34] and computerized tomography (CT) scanning. Although ultrasonic scanning is relatively quick to perform, and can detect small defects if the appropriate wavelength is used, it has important drawbacks when compared to CT scanning. The main advantage of CT scanning for the study of damage in composites is that it offers a higher internal 3D resolution of the specimen. Additionally, ultrasound scanning has difficulties providing clear information about multiple damage zones when they are aligned one behind the other in the path between the transmitter and the receiver, but CT scans are not affected by this phenomenon since projections are taken from multiple angles and then a 3D image is reconstructed.

Within the CT scanning technique, there are different methods to visualize the damage inside a CFRC specimen. The simplest method is color thresholding. This method consists of partitioning the greyscale of a CT scan into multiple divisions to separate regions in the scan by their density, then, a different color is assigned to each region for visualization. In the case of composites, this allows to calibrate a greyscale range for air and use it to detect delaminated areas and cracks based on their

location in the composite. This method was used by Chaeyoung et al. [35] to study the damage modes in a single-edge notched symmetric cross-ply laminate. Another method consists of submerging the specimen in a low viscosity dye penetrant that is highly visible in X-ray scans given enough time for the liquid to penetrate into the cracks and delamination areas. Then, the specimen is removed from the dye penetrant and a CT scan is taken. This method allows to clearly visualize the cracks, and it is relatively easy to follow. On the other hand, some drawbacks are that it does not allow to observe internal damage zones that do not have a connection to the outer surfaces of the specimen because the liquid cannot reach them. Additionally, due to the invasiveness of this method, once a specimen has been impregnated and scanned, it typically cannot be loaded and scanned again for observations of progressive damage as it would be desirable in fatigue studies for instance. Hong et al. [36] used this method to complement the in-situ CT scans of a single-edge notched cross-ply specimen presented in [35] and found delamination zones that were not visible from the in-situ observations. The fact that delaminations were not found in the in-situ observations was attributed to them not opening up enough to be observed using the thresholding technique and emphasizes the need for a better experimental inspection method that allows to observe this important damage mode.

Another method to visualize internal damage in a composite is Digital Volume Correlation (DVC). A detailed review of the technique can be found in [37]. The technique is similar to the commonly used Digital Image Correlation (DIC) method. DIC has allowed researchers to gain deep insight about the strain distributions that form in a composite even at a fiber level, as was done by Mehdikhani et al. in [28]. This level of insight is greatly useful in understanding the cracking initiation process in composites, however, it has limitations because it only provides measurements at the surface of the specimen, as opposed to DVC which allows to compute the strain field of a specimen at any plane of interest including internal plies. If the scans used in the DVC analysis are of enough resolution to clearly resolve the microstructure of the specimens, it is possible to use them directly for DVC analysis, avoiding the need to speckle the specimens with nanoparticles or some other invasive technique that can affect the damage mechanisms. DVC also offers the advantages of providing information about the redistribution of strains upon opening of cracks and delamination zones and allows to observe internal cracks that do not have a direct connection to the outer surfaces as opposed to observing cracks from CT scans using dye penetrant. These advantages allow for a better understanding of the damage mechanisms in a composite. The DVC technique was used successfully by Lee et al. [38] to study the strain field in a double-edge-notched $[+45_2/-45_2]_s$ specimen. Ferraro et al. [39] used DVC to study the residual damage after folding and unfolding a prototype self-deployable shell structure made of plain weave Astroquarz. Mehdikhani et al. [40] successfully demonstrated that DVC can be used to observe matrix cracking in laminated composites using a double-edge-notched cross-ply laminate.

The purpose of this chapter is to present a detailed study of the damage initiation mechanisms of a single-edge notched cross-ply laminate [90/0/90] using DVC to serve as a verification case for PFA models. The chapter is organized as follows. In section 2.2, experimental DVC results of the specimen at different points as it is loaded in tension are shown and discussed. Then, in section 2.3, Finite Element (FE) studies are shown to support the interpretation of the results shown in 2.2. Finally, concluding remarks that summarize the main findings are reported.

3.2 Experimental details and results

3.2.1 Specimen characteristics

The material used to manufacture the specimens was a T800H/3631 prepreg system by Toray cured in a hot press. The ply thickness is approximately 0.12mm. Single-edge notched rectangular specimens were cut from the cured panel using a waterjet cutter to a size of 45mm in length, 9mm in width, and a notch radius of 0.5mm. Fiberglass tabs were glued at the ends of the specimen using epoxy adhesive for a smooth load transfer from the grips to the specimen. The gage region length was 15 mm. A diagram with the specimen geometry is shown in Figure 22. Some specimens were first tested to failure to observe the global response of the specimen. The strain in these tests was measured using Digital Image Correlation (DIC). To be able to conduct the DIC analysis, these specimens were speckled as shown in Figure 22.

3.2.2 Experimental procedure

The experimental procedure followed in this study is based on the one that had been validated in [21], and is explained here for convenience. A Deben CT5000 station was used to load the single edge notched specimens described in section 2.2.1 inside a Zeiss Versa 520 µCT device. The specimens were loaded stepwise in increments to several levels around the damage initiation point at the tip of the notch. At every load level, a µCT scan of 1932x1464x967 voxels was collected in-situ as the load was held fixed (further details in section 2.2.4). Using the open source code FIDVC [41], a DVC analysis of the series of scans was performed. From the strain redistribution that occurred between the scans, the damage initiation mechanisms in the composite were studied.

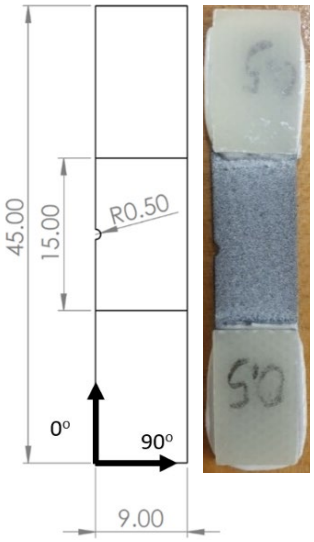

Figure 22 Specimen geometry (dimensions in mm)

To perform the DVC analysis, first the raw scans were registered using the image processing toolbox from MATLAB 2022 allowing only rigid body transformations. In the registration, the scans were aligned with the orientation of a reference scan taken before any load was applied. The correlation stage was done using the open source code FIDVC [41] with an interrogation window of 128x128x64 voxels. FIDVC uses a fast Fourier transform based cross correlation formulation in combination with

the iterative deformation method to calculate the 3D displacement field of each scan in relation to its reference unloaded state. From the 3D displacement field, the displacement gradients and the strain fields were computed using a post-processing MATLAB code developed in house. Using this code, the images presented in section 2.2.4 were generated.

3.2.3 Global quasi-static response

First, the global response of the specimen was observed to determine appropriate points at which loading could be paused for DVC analysis. DIC was used to measure the strain on one of the outer surfaces of the specimen. A summary of the global response is shown in Figure 23. In this test, the specimen was loaded in tension along the Y axis. It can be observed from the force-strain curve that the response of the specimen is mostly linear until the point of final failure. At approximately 1 kN, the first transverse cracks on the outer 90 plies can be observed near the notch in the DIC analysis. From this point onwards, additional transverse cracks appear gradually at random locations along the specimen's gage region until final failure of the specimen. Final failure happens when a main crack transverse to the loading direction starts at the notch and propagates horizontally through the width of the specimen driven by fiber breakage in the 0 ply. This main crack causes the specimen to break in 2 parts, preventing it from carrying any load. It is important to note that the previous observations are limited by the resolution and field of view used, as well as by the technique used (DIC). It is impossible to guarantee from surface measurements of the whole specimen whether delamination or splitting of the inner 0 ply has occurred at any given point, or even if the transverse cracks in the outer plies had already initiated before they could be detected but were not visible because the resolution was not high enough. Therefore DVC measurements were taken at fractions of the load at which cracking was first observed in the DIC analysis to be able to track the damage initiation mechanisms closely. The loads chosen for the DVC analysis were 0.30, 0.50, 0.55, and 0.60 kN.

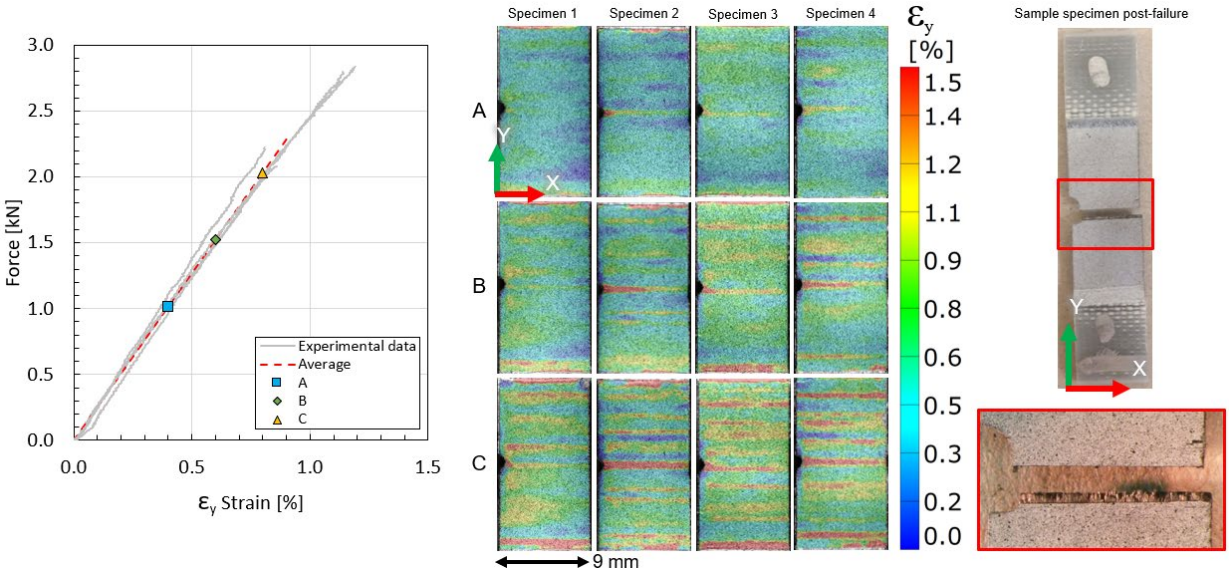

Figure 23 Global response of single-edge notched cross-ply specimens

3.2.4 DVC results

In Figure 24, the DVC results obtained at 0.30, 0.50, 0.55, and 0.60 kN are shown. At each load, the transverse strain in each ply is shown from 2 different views. The transverse strain ε_y in the front 90 ply (centered at z=t, where t is the thickness of a single ply) is shown in views 1 and 2. Similarly, the transverse strain ε_y in the back 90 ply (centered at z=-t) is shown in views 1 and 3. From these views (1-3), cracking in the outer 90 plies can be observed. The transverse strain ε_x in the 0 ply (centered at z=0) is shown in views 4 and 5. From these views (4&5), splitting in the 0 ply can be observed.

First, in the scan at 0.3 kN, no significant strain concentrations can be observed. The strain field within each ply looks mostly uniform, indicating that no cracks have developed yet. At this point the specimen is in the uncracked elastic regime.

In the scan at 0.5 kN, a noticeable difference between the ε_y strain field in the ply at view 2 and the ply at view 3 can be observed. This difference is attributed to the formation of a delamination zone at the interface between the 0 ply and the 90 ply at view 3. The indication that this is the first interface to begin to delaminate is that the ε_y strain in this 90 ply (90 ply at view 3) is higher. If the 3 plies were free to deform independently, the 90 plies would have a higher average ε_y strain at the location inspected, therefore, when decoupling between the plies begins due to delamination, the ε_y strain in the 90 ply tends to suddenly increase. This point is discussed in further detail in section 2.3.2. The difference is not significant enough to be certain that delamination in this region has fully developed but it indicates that the process zone in the matrix at the interface has begun to form. Other important things to notice from this scan is that no splits or cracks have formed in the plies. This can be verified visually by the lack of openings between fibers.

In the scan at 0.55 kN, it can be observed how the delamination zone that had begun to form in the previous scan fully developed by now, leading to an abrupt load redistribution. As a product of the load redistribution, the interface between the 90 ply at view 2 and the 0 ply becomes the only one constraining the high tensile deformation that the 0 ply has a tendency for in the X direction. This point is also discussed in further detail in section 2.3.2. The latter results in a large increment in the shear stress at the interface between these plies (the 0 ply and the 90 ply at view 2), which leads to delamination. The fact that both interfaces have delaminated can be verified by the large increment in the ε_y strain of both 90 plies for a small increment in load, for the reasons explained in the scan at 0.50kN. Once both interfaces have delaminated, the 0 ply can deform freely. The transverse stresses in the 0 ply upon load redistribution exceed the strength of the matrix and causes the ply to split where the stresses are highest. This split crack is clearly visible in Figure 24 at the lower part of the notch. After splitting, the strain concentrations that had been observed in the scan at 0.50 kN relax. Something important to notice from this scan is that the strain in the 90 plies is concentrated in bands along the fibers. These bands are visible to a lesser degree than the scan at 0.3kN, therefore they can be attributed to local material inhomogeneities in the microstructure such as fiber clustering. This point is also discussed in further detail in section 2.3.1.

In the scan at 0.6 kN, the beginning of transverse crack formation can be observed near the notch in both of the 90 plies. Additionally, the strain concentrations in the 0 ply increased again compared to the scan at 0.55 kN, indicating that the split crack has stopped growing for now, and this region has begun to carry more load.

To summarize, the damage initiation mechanisms observed from the DVC analysis are as follows; first, the incompatible deformations between the 0 and the 90 plies lead to high shear stresses at the ply interfaces near the notch. Because of the differences (scatter) in strength between the two interfaces likely from the manufacturing process, one interface delaminates first, but quickly after the load redistributes, the other interface also fails and the 0 ply splits. Lastly, after a small increment of load, transverse cracks develop in the outer 90 plies.

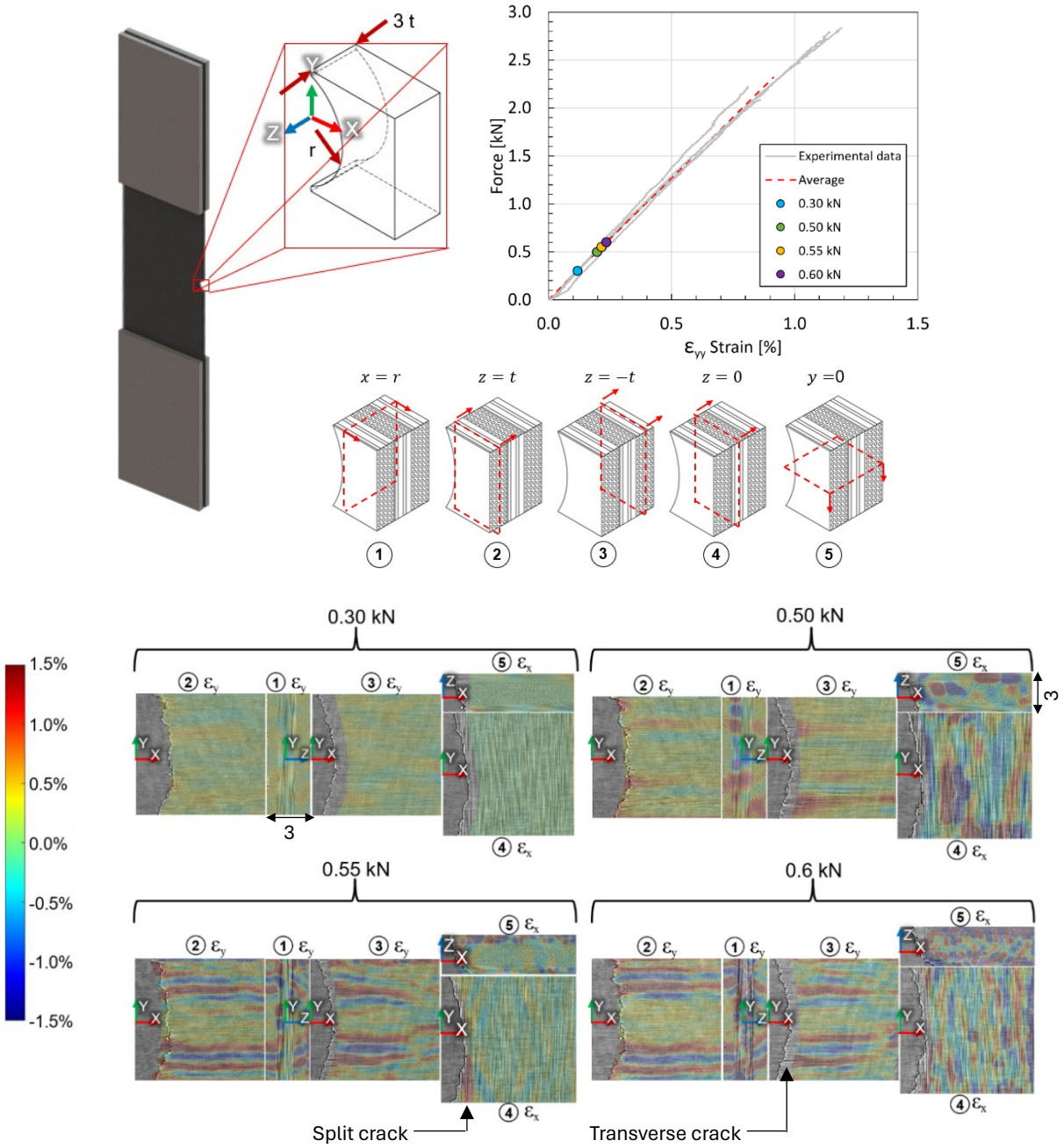

Figure 24 Digital Volume Correlation results of single-edge notched cross-ply laminate

3.2.5 Dye penetrant results

To verify that the cracks inferred from the DVC analysis in section 2.2.4 were indeed present, after the test, the specimen was submerged in dye penetrant and a CT scan was taken. In Figure 25, the dye-penetrant-enhanced scans along with the DVC images at 0.60 kN are shown. From the figure, it can be clearly observed that the transverse cracks in the 90 plies and the splitting in the 0 ply are present as inferred from the DVC analysis. However, no clear sign of delamination was observed from the dye-penetrant-enhanced scans. This is potentially because the test was stopped soon after delamination had just begun and thus the delaminated area had not opened sufficiently for the dye to penetrate. This phenomenon was observed in a similar test presented in [36].

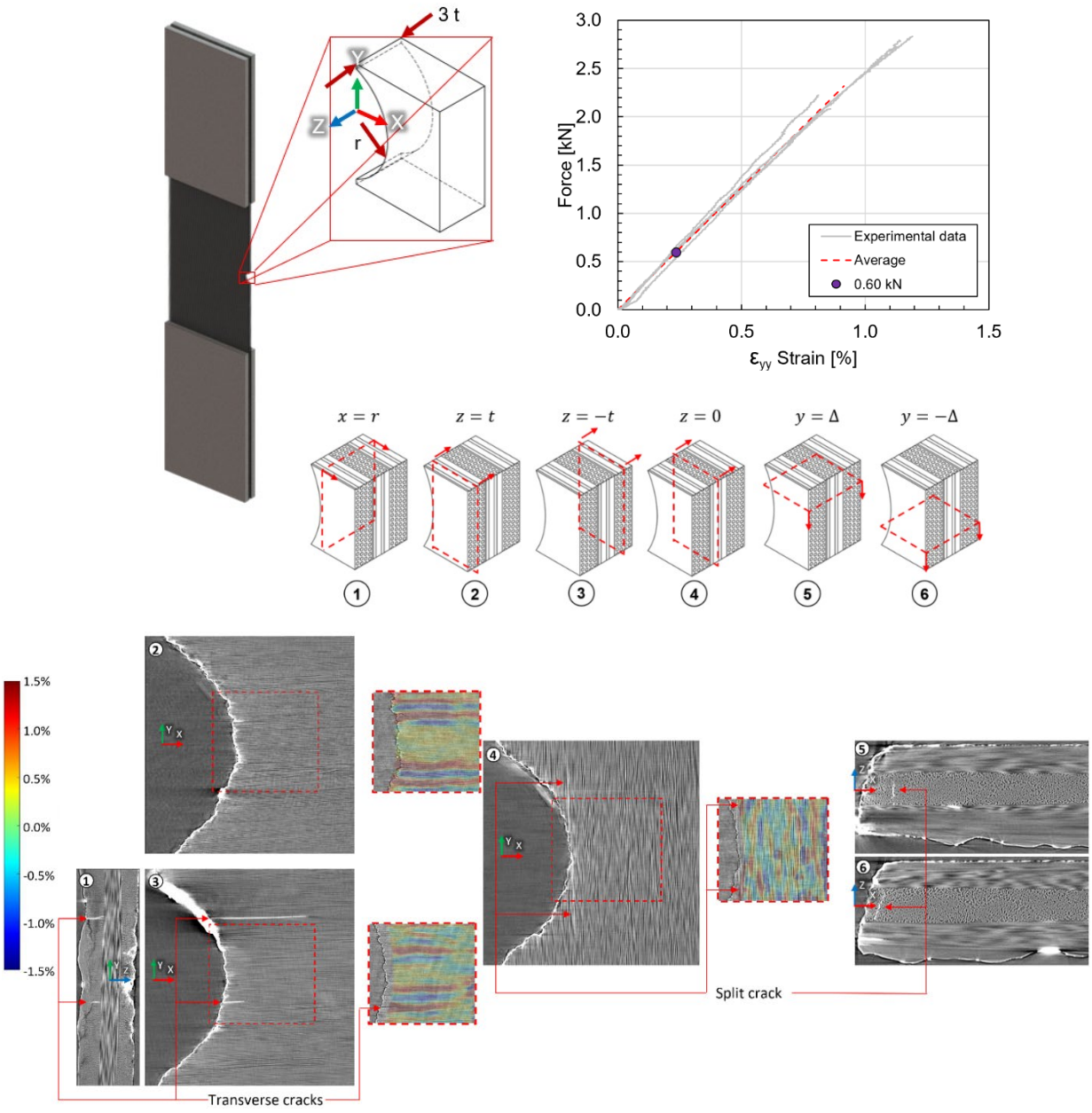

Figure 25 Dye-penetrant-enhanced CT scans of specimen after being loaded to 0.60 kN

3.3 Simulation results

To verify that the results observed in the DVC analysis are physically meaningful and not caused by artifacts from the CT scan, a series of finite element models were constructed to observe different aspects of the results. The first analysis is a micro-macro model, where the strain field of the specimen prior to damage formation is studied at the scale at which observations are made. Then, from a mesoscale model, the strain field of individual plies deforming independently are analyzed to understand the trends that each ply has, which helps identify when delamination has occurred.

3.3.1 Micro-macro model

To verify the strain fields observed in the DVC analysis prior to damage initiation, i.e. the scans at 0.3 and 0.5 kN in Figure 24, a Finite Element (FE) macro-micro model of the specimen's gage region was constructed using first order continuum elements with a hex-dominated mesh. First, a quarter of the [90/0/90] laminate was modeled ply by ply using a homogeneous, linear elastic, and orthotropic material behavior. Perfect bonding between the plies was assumed. The specimen's symmetry about the XY and XZ planes was leveraged to reduce the model size. The top of the gage section was assumed to be clamped and a displacement U_y was applied in tension to reach a global strain of 0.5%. Since the simulation is linear elastic, and the main interest of this simulation is to observe the spatial distribution of the strain field and not the magnitude, the exact global axial strain applied is not critical, and 0.5% was chosen for convenience. Symmetry boundary conditions were applied at the planes of symmetry of the specimen (XY and XZ). Partitions were made near the tip of the notch to delimit a small region similar in size and location to that analyzed using DVC and the displacements at the boundaries of this region were measured. The elastic properties of the T800H/3631 system at a fiber volume fraction of 0.45 were obtained from [42]. These properties are listed in Table 4.

Table 4 Elastic properties of homogenized T800H/3631 system at 0.45 fiber volume fraction

Property	Value
E_1	169 GPa
E_2	9.62 GPa
G_{12}	4.50 GPa
v_{12}	0.349
v_{23}	0.490

A microscopic model of the small region near the tip of the notch was created. In this model, the fibers and matrix were modeled explicitly, however, to obtain a model that was manageable computationally, the fibers were scaled up in size by a factor of 3. It should be emphasized that the objective of this FE model is to verify that the strain field patterns observed in the DVC analysis are indeed caused by the physics of the test and to discard the possibility that they are caused by artifacts from the inspection technique. Although the fibers have been scaled, they are still of comparable size within the same order of magnitude, therefore it is reasonable to assume that the observed behavior would be similar for a model with the correct fiber size. At the boundary surfaces of the micro model, the displacements measured from the macro model at the partition surfaces of the small region near the tip of the notch were imposed. The only surface where the displacements

were not imposed and symmetry boundary conditions were used instead, was that on the XY plane. The latter simplification was done to make the model more computationally efficient. The details of the macro-micro model are shown in Figure 26.

To determine the properties of the matrix and the fibers in the micro model, first, the matrix was assumed to have an isotropic material behavior and the fiber was assumed to have a transversely isotropic material behavior. Using the properties in Table 4, a gradient-decent optimization algorithm in combination with a micromechanics analytical model was used to find the properties of the constituents that best matched these homogenized properties. The micromechanics model used was the Concentric Cylinder Model-CCM [27]. The obtained properties of the constituents are shown in Table 5. It must be mentioned that when running the optimization algorithm, the fiber volume fraction was also treated as a variable to be found. The fiber volume fraction obtained using the optimization algorithm was 0.57.

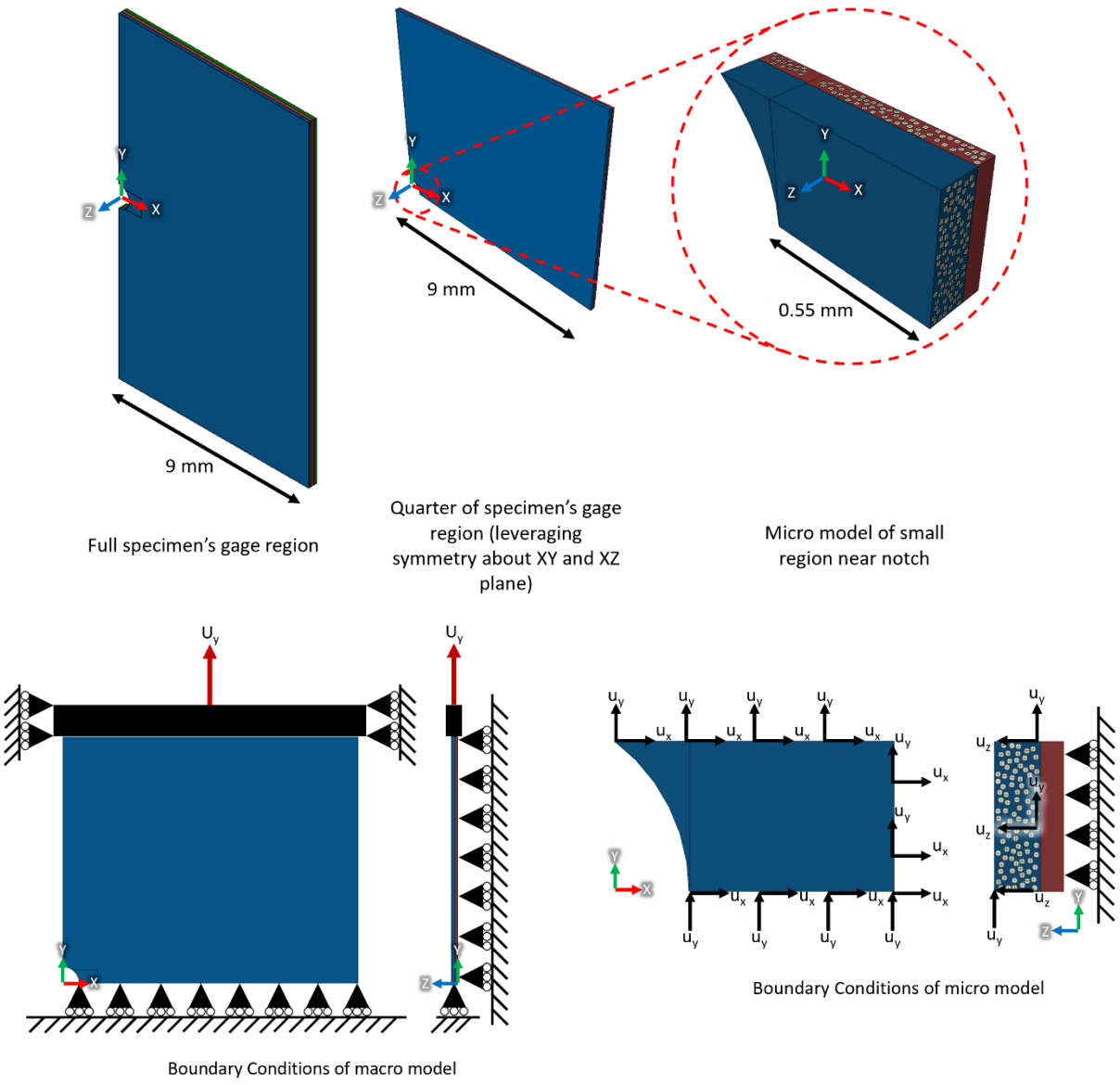

Figure 26 Macro-micro model details

Table 5 Constituent properties of T800H/3631 system

Constituent	Property	Value
Fiber	E_1	294 GPa
	E_2	184.50 GPa
	G_{12}	130.54 GPa
	v_{12}	0.286
	v_{23}	0.349
Matrix	E	3.67 GPa
	v	0.442

To validate the properties obtained in Table 5, the CCM method was used to calculate the homogenized properties obtained using these constituent properties and the fiber volume fraction found via optimization and comparing them against the homogenized properties reported in [42]. Both sets of properties are shown in Table 6. It can be observed that the sets are very close to each other. Apart from v_{23}, all the properties are within 10% of the values reported in [42], therefore, the constituent properties obtained via optimization were considered acceptable and used in the model shown in Figure 26. It should be noted that although the error obtained using CCM for v_{23} is large, this property of the homogenized composite has a small influence on the global response for the loading cases investigated in this study. Thus, the mismatch in v_{23} obtained with CCM is considered to be acceptable.

Table 6 Comparison of homogenized properties reported in [42] and the ones obtained using CCM

Property	Value reported in [42]	Value obtained using CCM	Error
E_1	169 GPa	169 GPa	0%
E_2	9.62 GPa	10.15 GPa	6%
G_{12}	4.50 GPa	4.50 GPa	0%
v_{12}	0.349	0.349	0%
v_{23}	0.490	0.238	51%

For placement of the fibers in the micro model, the Random Sequential Adsorption (RSA) algorithm [22] was used. A fiber volume fraction of 0.57 was aimed when placing the fibers such that the global ply properties matched those in Table 5, however, due to the fiber scaling needed to keep the model at a manageable size, the average fiber volume fraction obtained was 0.30. Although this difference causes an undesirable discrepancy in stiffness between the macro and the micro models, the main features of the model are preserved. Thus, the micro model can still be used to make a qualitative verification of the undamaged strain field observed in the DVC analysis (scans at 0.30 and 0.50 kN) but the results should be interpreted with caution. A mesh size corresponding to 50% of the scaled fibers (diameter) was used.

The results of the micro model are shown in Figure 27. It can be observed that, similar to the strain field obtained from the DVC analysis (shown in Figure 24), bands of strain concentration form in each ply influenced by the local fiber clustering. These bands run parallel to the fiber direction, and

manifest in the transverse strain component, i.e. ε_y for the 90 plies and ε_x for the 0 plies. At this scale, the features of the strain field are significantly more dominated by effects from the microstructure than they are by strain concentrations expected from a macro model with *homogeneous* composite properties. These results are in accordance with the strain field observed in the DVC analysis. Additionally, these results suggest that damage initiation is heavily influenced by the stress concentrations introduced by features of the local microstructure at critical locations. The latter observation has important implications for mesoscale PFA models, since it implies that they need to account in some way for this effect to predict damage initiation accurately.

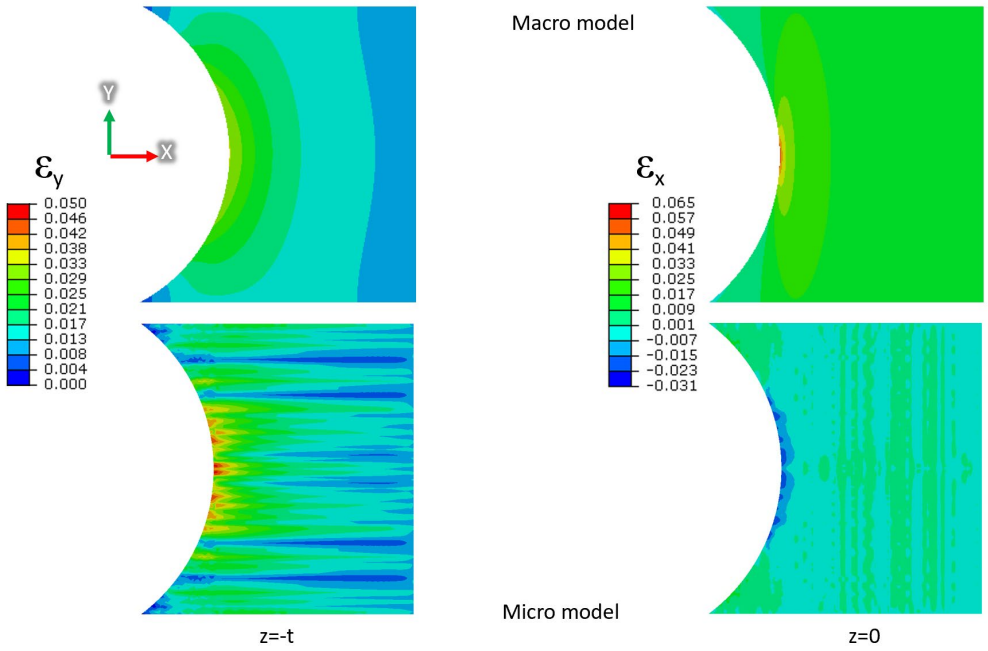

Figure 27 Macro-micro model results

3.3.2 Independent deformation of each ply

To better understand the deformation state that each ply in the single-edge notched [90/0/90] laminate tends towards when loaded in tension, the strain fields of an isolated 0 ply and an isolated 90 ply loaded in tension were analyzed. A model for each ply was created using first order continuum elements, and the mesh was sized to be 1/30 the size of the notch. An implicit static solver was used. Similar to the model presented in section 2.3.1, these models were used exclusively for a qualitative analysis, thus, 0.5% global strain was used for convenience. The strain fields are shown in Figure 28. A detailed view of a small region near the tip of the notch is also shown for clarity.

Regarding the ε_y strain component, it can be observed that although the 0 ply has a larger strain concentration at the tip of the notch compared to the 90 ply, this concentration is localized in a smaller region. The 90 ply clearly has a larger average strain over a greater region near the notch. Therefore, it makes sense that when the interface between these 2 plies delaminates, a jump in this strain component at the region near the tip of the notch is observed as the average strain grows.

Regarding the ε_x and ε_{xy} strain components, it can be observed that the 0 ply has large strain concentrations on the edge of the notch at approximately 30 degrees with respect to the x axis, while

the 90 ply does not. Therefore, it makes sense that while the 0 ply is still coupled with the 90 plies, this trend is limited by the stiffness provided by the 90 ply in the x direction but as soon as the interfaces delaminate, the 0 ply can deform freely and splitting occurs at the locations of strain concentrations.

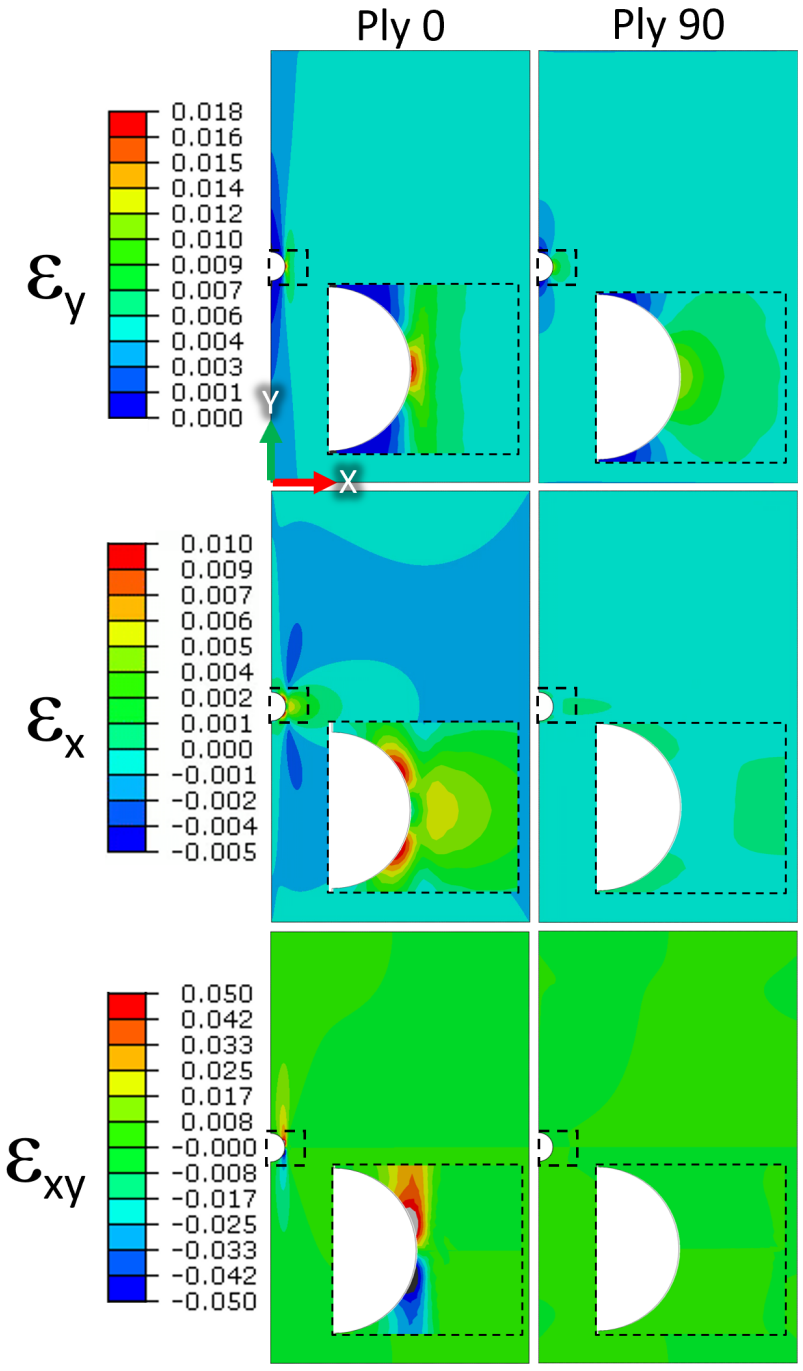

Figure 28 Elastic deformations of 0 and 90 plies under tension loading (0.5% global strain)

3.4 Conclusions

In this chapter, the damage initiation in a single-edge notched cross-ply [90/0/90] composite laminate loaded in tension was analyzed experimentally using DVC. The DVC implementation was without adding external agents to produce a speckle pattern. From the DVC results, it was observed that the first damage mode to activate in the experiment was delamination of one of the interfaces at approximately 24% of the ultimate load in a small region near the tip of the notch. The delamination of the first interface led to a stress redistribution that quickly caused delamination of the second interface and splitting of the internal 0 ply. The last damage mode to be observed was transverse cracking of the 90 plies at approximately 26% of the ultimate load. In the dye-penetrant-enhanced CT scans, the transverse and split cracks observed in the DVC analysis were verified, however, the delamination areas were not found. This is attributed to the delamination area not opening enough for the dye to penetrate, which is similar to that reported in [36]. To validate that delamination had indeed occurred, FE analysis were conducted to better understand the deformation state that each ply tends towards when loaded independently and they were compared to the DVC strain fields. The latter helps demonstrate that when delamination is interpreted to have occurred, the local strain fields of each ply show close resemblance to the strain fields of isolated plies deforming independently.

Chapter 4 – Multiscale progressive fatigue damage model

4.1 Introduction

Composite materials are favored for use in weight-critical aerospace structural applications. These materials offer outstanding strength and stiffness-to-weight ratios when compared to metals. Despite this advantage, the potential of composites is seldom fully exploited. The advancement of computational tools that allow to predict failure of composites reliably and efficiently would enable better designs with these materials. One of the loading cases for which failure models of composites have the most room for improvement is fatigue.

Fatigue in composites is primarily driven by the continuous growth and interaction of matrix cracks and delamination zones. These damage modes affect the stiffness of a structure and can cause it to perform suboptimally, and, in some cases, it can even cause it to fail catastrophically. Fatigue of composites is a complex phenomenon, multiscale in space and time. To model it accurately, it is important to capture the development of microcracks that happen over long periods of time as well as macroscopic crack propagation that can happen in a fraction of a second. Therefore, a multiscale model is an appropriate method to predict reliable the fatigue life of aerospace composite structures.

Typically, fatigue models for composites in the literature lack at least one of the following requirements: they are either hard to generalize to a wide range of laminates with different stacking sequences without requiring the characterization of an impractical number of model parameters, or they are computationally inefficient. For example, Van Paepegem et al. [1] developed a 1-dimensional Finite Element (FE) model for composites using plain-woven glass/epoxy specimens loaded uniaxially. They proposed a fatigue law with 5 fitting constants to predict the loss in stiffness

and strength of each element in the model as a function of the maximum stress reached in each cycle and the accumulated damage. Then, they determined the fitting constants via inverse modeling. These 5 constants, however, were specific to this stacking sequence, mean load, and load amplitude. It can be noted that, although this approach can be highly efficient from a computational standpoint, without proper adaptation, it cannot be used to predict the fatigue life of composites with a general layup subjected to a general multiaxial state of stress. In the other extreme, models like the one proposed by Carraro et al. [43] offer a high level of accuracy by tracking the growth of individual cracks and delaminated areas and accounting for their effect on the stiffness of the structure via analytical methods. Despite the accuracy offered by this type of model, their use in engineering applications is limited due to the difficulty of implementing them in a computationally efficient way with finite element (FE) frameworks that allow to study structures of complex geometries.

In this chapter, a novel multiscale FE model that offers a suitable balance between accuracy and efficiency to be implemented in engineering applications is proposed. The model achieves this balance by carefully integrating several multiscale resources available in the literature and by making key simplifications that allow it to be used in a computationally efficient way. Additionally, the model implements a neural network to speed up multiscale calculations. The model is currently still under development, and the features presented herein are an initial approach, improvements will be made as the model continues to be validated against experimental data.

4.2 Model description

4.2.1 Formulation of fatigue degradation definition and characterization from experimental data

The main multiscale resource used in the proposed methodology in this chapter is NCYL (N-Layer concentric cylinder model). This model was introduced by Zhang and Waas in [44] and it is a multi-scale computational mechanics framework for progressive failure modeling of composite structures. This framework allows to compute analytically the strains in the matrix of a composite Representative Unit Cell (RUC) as a function of the macroscopically homogenized values obtained from a classical laminate theory analysis or a similar method. Leveraging this capability, the apparent degraded matrix properties of a composite due to microcracking can be characterized as a function of number of cycles and loading characteristics. By relating the damage in the composite to the matrix, it is possible to make the characterization independent of the specific laminate that was used, and generalizable to other stacking sequences. This approach was proven to be feasible in [45].

In [45], Davison and Hasanyan conducted residual strength tests of $[\pm 45]_{(2s)}$ laminates loaded cyclically at different fractions of the laminate's quasi-static strength. They used a prepreg T800S/3900-2B material system from Toray with a toughened interface. In each test, they observed a structural response like the one shown in Figure 29. 3 distinctive regions can be noticed. The initial non-linear response in region I was attributed to microcracking. Region II was attributed to the formation of macroscopic cracks along the fibers in all plies. Region III was attributed to the stiffening of the laminate due to fiber reorientation. This stiffening is achievable in these laminates due to the toughened interface which delays delamination.

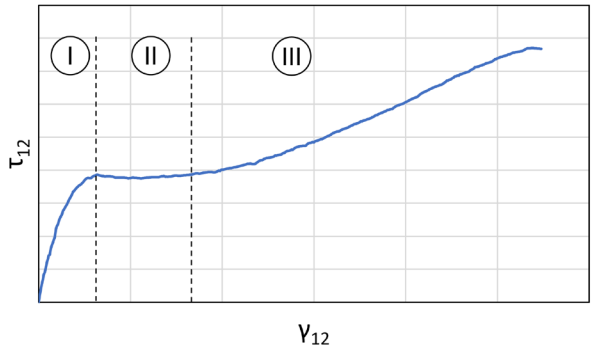

Figure 29 Typical structural response of $[\pm 45]_{(2s)}$ laminate loaded in tension to failure

When fatiguing the specimens, the loading conditions that Davidson and Hasanyan used were as follows: a minimum load of 0, a maximum load of 70, 85, 90, and 100% the plateau load of a quasi-static test, and a maximum number of cycles of 150 thousand. Using NCYL, they were able to obtain equivalent matrix stress-strain curves from the composite residual strength curves measured. Following the process described in [45], these equivalent matrix stress-strain curves were calculated independently, and the results obtained are shown in Figure 30. The curves shown in the figure were truncated at the end of region II because up to this point the structural response is dominated by the intraply properties. Beyond this point it does not make sense to calculate the equivalent matrix stress-strain response because the effects from the toughened interface and the fiber realignment dominate the structural response. There are 3 key observations that can be made about the curves shown in the figure that were used to formulate the model proposed in this chapter. First, all curves tend to meet at the end of region II, regardless of the load level that the specimens were cycled at. Second, all curves tend to approximately follow a bilinear behavior. Third, as the number of cycles increases, the stress-strain curve tends to a straight line from the origin to the end of region II in all load levels.

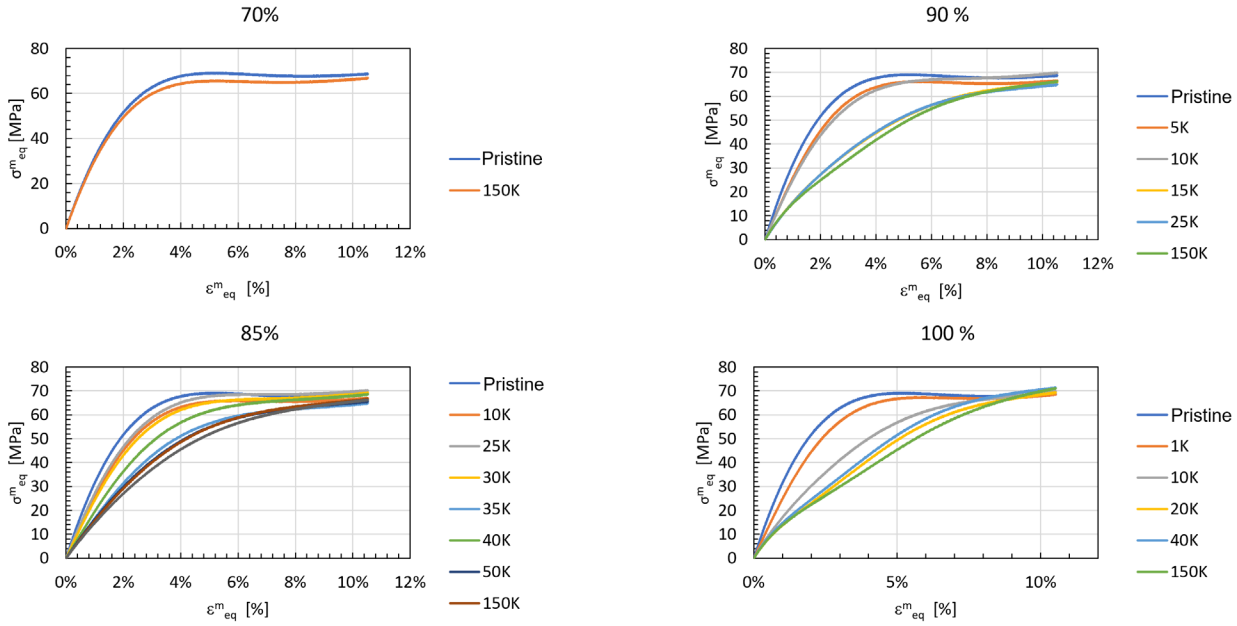

Figure 30 Equivalent matrix stress-strain response (residual strength curves)

The observations mentioned previously were leveraged to formulate a simple definition of fatigue degradation. First, a bilinear approximation was fitted to the stress-strain plot of the pristine sample. Keeping the same end point of region II and the same length of the first arm of the pristine fit, the best bilinear approximation for the rest of the curves was found. In Figure 31, the definition of degradation previously described is illustrated. L_1 in the figure indicates the first arm of the pristine fit which stays the same length for all fits. Also, the star marks the end of region II in the pristine fit, which is also assumed to remain unchanged for all fits.

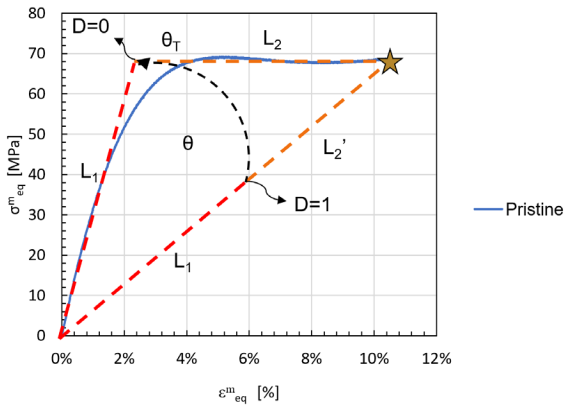

$$D = 1 - \frac{\theta}{\theta_T}$$

Figure 31 Definition of degradation

In the figure, the bilinear approximation for the case when degradation (D) is equal to 0, and when it is equal to 1 are shown. θ_T corresponds to the total angle between the fits for minimum and maximum degradation. For any other curve, the angle (θ) that best fits the data was found and then used to calculate the corresponding D using the equation given.

Using this definition of fatigue degradation, the progression of degradation was characterized for each fatigue load from the data presented in Figure 30. This progression is shown in Figure 32 A. To process this data into a more practical form, a trilinear approximation was fitted. For cycles beyond the ones available in the data, the degradation was assumed to remain unchanged. The processed results are shown in Figure 32 B.

It is important to note that in the specimens used in [45], it is reasonable to assume that the stress is uniform throughout the gage region, however, in a real structure there are typically stress risers that lead to an uneven stress distribution, and an uneven fatigue degradation. To be able to use the data shown in Figure 32 in a fatigue model, the degradation growth per cycle was characterized as a function of fatigue degradation and maximum stress. For values in between the percentages characterized experimentally, linear interpolation was used. For cases when the maximum stress is below 70%, no degradation growth was assumed. When implementing this approach to calculate the composite response, another multiscale method known as the Concentric Cylinder Model (CCM) [46] was used to calculate the homogenized degraded properties of the composite from the degraded matrix properties and the pristine fiber properties. The fiber is assumed to keep its pristine properties unless the criterion for fiber failure is met. More details are provided in the following sections. It is important to note that because of the nature of the data, the fatigue degradation

function developed depends only on the maximum stress and degradation level, but not on the mean stress or the frequency. Dependence on these variables will be studied in future work.

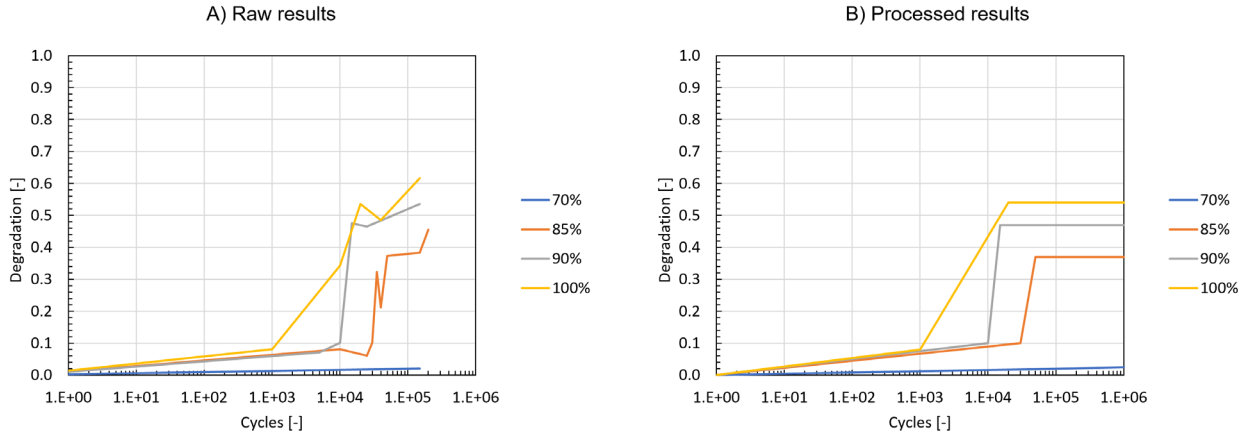

Figure 32 Fatigue degradation progression

4.2.2 Use of a neural network to accelerate NCYL calculations

Although NCYL by being an analytical method offers great computational advantages over an equivalent Finite Element (FE) Representative Unit Cell (RUC) model with comparable resolution it can still be too slow to incorporate directly into a fatigue model. The reason is because when using NCYL, the equivalent matrix strain needs to be calculated at multiple points of the RUC and then averaged. Each of this calculations requires inverting a relatively large matrix, which is computationally expensive. Moreover, because a fatigue simulation requires modeling multiple cycles, this computational cost multiplies.

From a global perspective, when using NCYL, the input to the model are 6 composite strain components (apart from the material properties), and the output is an average equivalent matrix strain. Therefore, it is reasonable to assume that the analytical model can be replaced using a neural network. When incorporating the degradation variable D, the total number of inputs for a given material system would be 7. A diagram of the described neural network is shown in Figure 33.

It should be noted that training such a neural network for every possible scenario can be highly challenging since the number of combinations are practically infinite, even limiting the use of the neural network for a single material system. One approach could be to use large volumes of data sampled using methods like the Latin hypercube, however this could still be a long process. The goal for the model in this chapter is to serve as a proof of concept, therefore, instead of aiming to train the neural network for every possible scenario, the scope was bounded to training it for problems of notched thin cross-ply laminates.

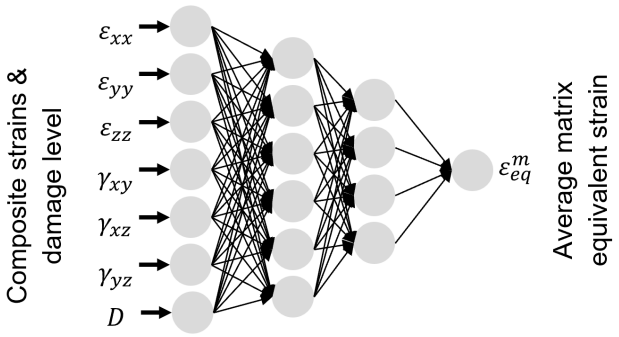

Figure 33 Neural Network to replace NCYL calculations

To train the neural network, 3 problems were chosen: an unnotched specimen, one with a single-edge notch, and a last one with an open hole. All specimens had a [90/0/90] stacking sequence, were 15mm long, 9mm wide, and had a notch radius (if applicable) of 0.5mm. A diagram of the specimens is provided in Figure 34. First, FE models of these specimens were constructed using the homogenized properties of the material system used in [45]. Each model was loaded in tension to a global 1% axial strain, and the composite strains were obtained. This procedure was repeated for 11 different degradation values (33 simulations in total) from 0 to 0.99, assuming that the degradation was the same throughout the specimen. For each level of degradation, the composite strains from the 3 problems were combined, then an Independent Component Analysis (ICA) was performed, and 6 ICA components were obtained. 100 datapoints along each ICA component were generated, for a total of 600 datapoints per degradation level, and a global total of 6,600 datapoints to train the neural network. The equivalent matrix strain of these 6,600 datapoints were calculated separately using MATLAB, and used to train the neural network in TensorFlow. It should be noted that the approach of assuming that the degradation was the same throughout the specimen when generating these models was used merely for convenience. In reality, as mentioned before, when a notch is present in a structure, fatigue degradation is non-uniform. This approach, however, allows to easily generate sufficient points to train the neural network at different levels of fatigue degradation. In the future, this approach will be improved.

To test the accuracy of the neural network, the composite strains, and their equivalent matrix strains at different levels of fatigue degradation were calculated for a double-edge notched specimen as the one shown in Figure 34. The equivalent matrix strains were calculated using MATLAB, and using the neural network. The average difference between the calculated strains using both methods was of 3% throughout all degradation levels, however, calculation speeds using the neural network were observed to be up to over 1,000 times faster than the analytical calculations.

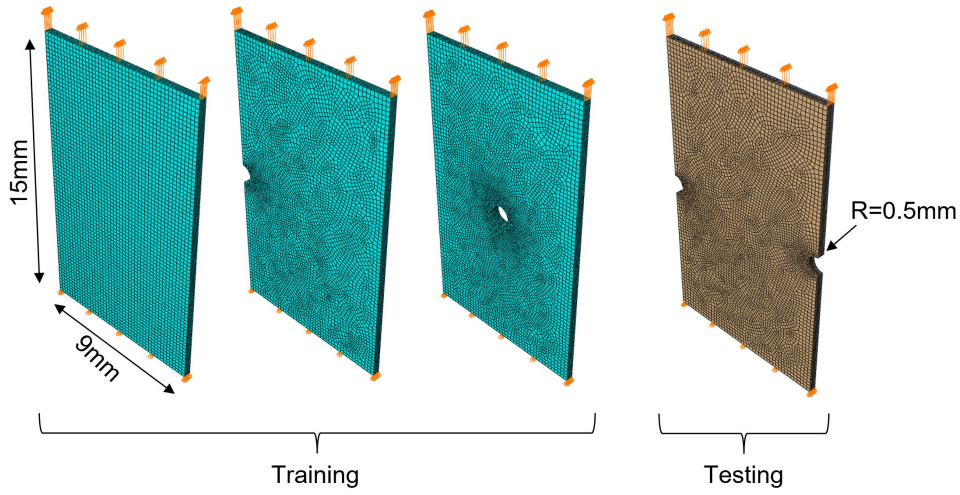

Figure 34 Training and testing problems to train neural network

4.2.3 Finite element modeling approach

As mentioned in the introduction, fatigue in composites is caused by microcracking that develops over long periods of time, but also by macroscopic cracks and delamination zones that can grow in a fraction of a cycle as stresses redistribute. To be able to model these damage modes, an approach that can capture them is required. An FE modeling method that was developed with these points in mind was the Semi Discrete Damage Model (SD2M), introduced by Nguyen and Waas in [15]. In this chapter, an FE approach inspired by SD2M is proposed. The model was developed in ABAQUS using 3D solid elements.

To capture macroscopic cracking, which typically develops along the fibers, plies were partitioned as shown in Figure 35. With this partition, a fiber-oriented mesh is obtained. The split regions in the partition are allowed to fail in fiber and matrix modes whereas the bulk elements are only allowed to fail in fiber modes. This way, sharp macroscopic cracks can be modeled in a semi-discrete way. Section 3.2.4 provides a more detailed description of how damage is modeled. Using the fatigue degradation function obtained in section 3.2.1, the homogenized effect of microcrack growth can be accounted for in both regions. On the other hand, when stresses grow beyond a certain point, macroscopic cracks can be captured thanks to the split regions. These split regions are particularly important to model the interaction between delamination zones and intraply macroscopic cracks. To capture delamination, the interface between composite plies is modeled using a thin isotropic ply of matrix. The properties of the matrix, including fatigue degradation and failure follow the same logic as the matrix in the split regions. This way, an additional characterization of a fatigue degradation function for the interface is not necessary.

4.2.4 Failure modeling approach

4.2.4.1 Matrix-mode failure

To account for matrix failure in the split regions and the interface plies of the model, a cohesive model with a linear softening curve was used. A sample shape of this curve is shown in Figure 36. Additionally, to account for strength variation at different points in the material, a scaling factor (SF) was introduced. This scaling factor represents the ratio of the transition point (bilinear model before

failure) in the modified curve with respect to the pristine value. When the scaling factor is 1, the matrix behaves like the bilinear models characterized in section 3.2.1, but if the scaling factor is lower, the transition point occurs earlier. Similarly, if the scaling factor is greater than 1, the transition point occurs at a higher strain following the initial stiffness. In either case, the slope of the second linear section, the strain to failure initiation, and the slope of the unloading curve are preserved in the current version of the model.

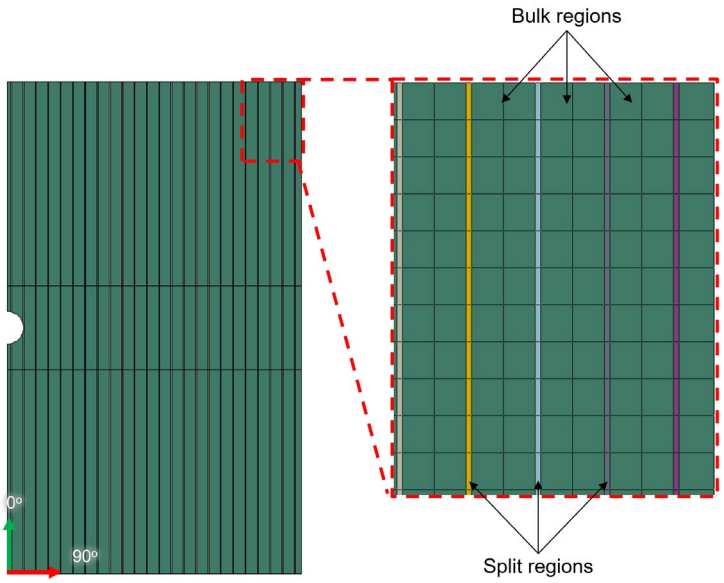

Figure 35 Finite Element modeling approach

In the FE model, each split region is assigned a random scaling factor. Each scaled unloading curve is taken as the pristine material behavior over which fatigue degradation is later applied. The probability distribution used to assign the scaling factor for each split region should be calibrated such that the crack density in the model is representative of experimental results. A detailed description of how this can be achieved is beyond the scope of this chapter.

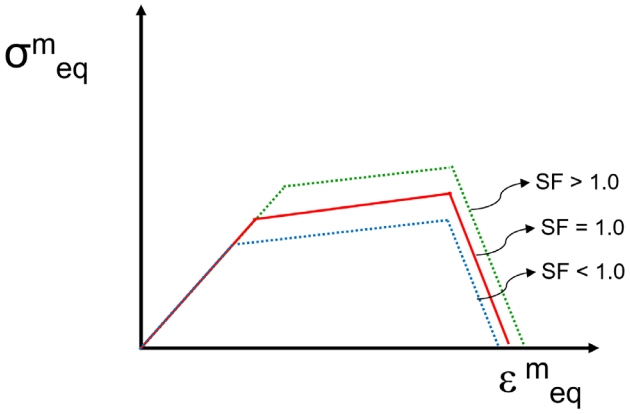

Figure 36 Matrix softening curve (not to scale)

Using this methodology to account for matrix failure has the advantage of allowing to easily calculate the corresponding unloading curves at the composite level for mixed loading using a single fracture toughness value. By combining the degraded secant matrix modulus with the pristine elastic modulus of the fiber using CCM, the unloading curves of the composite can be obtained. This single matrix fracture toughness value is a model parameter that still needs to be calibrated to reproduce experimental results. This will be done in future work. Additionally, in the current version of the model, the pristine fracture toughness is assumed to remain unchanged as fatigue degradation grows. This is merely for convenience. This assumption will be assessed and modified as needed in future work.

Once failure has initiated in an element, it is possible that the element does not fully fail. For simplicity, in these cases the fatigue degradation is assumed to not grow any further. Moreover, to model crack propagation due to cyclic loading, if the element does not fail after a given number of cycles (set by the user) from the resulting stress redistributions, the element is deleted.

4.2.4.2 Fiber-mode failure

Modeling fiber-mode failure with the framework proposed so far can be challenging. When a composite fails in the fiber direction, it displays some toughness and not an entirely brittle-like failure. This is because even if fibers brake, pieces of the bundle continue to be held by the surrounding matrix and thus, loads can still be transmitted. As can be noticed from the previous description, this phenomenon happens at the composite level and cannot be attributed to failure of the individual constituents.

To address this challenge, in the current version of the model, it is proposed that when the composite reaches a critical stress in the fiber direction, a more traditional cohesive model is used at the composite level. For simplicity, the unloading behavior is assumed to be dominated by the strain in the 11 direction (no mixed formulation), a linear unloading curve is assumed, and all the composite stiffnesses are equally degraded during unloading. Similar to the case of matrix-mode failure, once failure has initiated, fatigue degradation is assumed to not grow any further. Also, to model crack propagation due to cyclic loading, if the element does not fail after a given number of cycles (set by the user) from the resulting stress redistributions, the element is deleted.

It is important to note that during fatigue loading in structural applications, although fiber-mode failure can happen, it is typically rare until the end of the fatigue life. At this point, the stiffness performance of the structure is likely to already be significantly below acceptable levels, therefore, the proposed simple approach to model fiber-mode failure is considered to be reasonable. However, as for the rest of the assumptions proposed in the current version of the model, this assumption will be reassessed and modified as needed in future work.

4.2.5 Model integration

To implement the procedure previously explained, these steps were integrated into a user subroutine in ABAQUS. To model fatigue efficiently and avoid simulating every cycle explicitly, a cycle jumping approach was used. This approach consists of simulating explicitly only selected cycles and “jumping” the cycles in between. The jump between simulations is often made based on the stress level of the element with the fastest growing damage rate. This is how it was implemented by Van Paepegem and Degrieck in [1]. Determining the number of cycles to be jumped in this way requires

assessment of the stress level in all elements of the model, which can take a long time because each simulation needs to be terminated, the results file needs to be accessed, then a new simulation needs to be prepared based on the results and launched. This process is repeated until global failure is reached. Instead, in this chapter, it is proposed to determine a fixed jump size since the beginning and advance damage in each element independently within the subroutine, which allows to avoid the time-consuming process that would be necessary otherwise. An appropriate jump for this scheme can be determined by showing convergence of the results with increasingly smaller jumps.

At every increment within the simulation, the material response at a given integration point is calculated using the process shown in Figure 37. First, the strains are passed to the user subroutine by the ABAQUS solver, then an equivalent matrix strain is calculated using NCYL via the previously trained neural network. A corresponding secant matrix modulus is then determined. Using CCM, the homogenized properties of the composite are calculated. Using the composite strains and the homogenized properties, the composite stresses can be obtained. This process is repeated until failure of the element occurs.

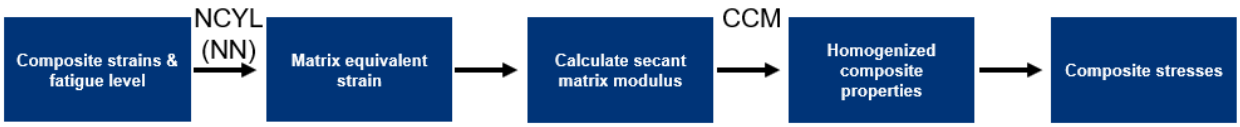

Figure 37 Evaluation of material response at each increment

4.3 Preliminary results

4.3.1 Quasi-static model

To evaluate the model, first, its accuracy in a quasi-static loading scenario of a single-edge notched cross-ply laminate was assessed. Although the model is intended to be used for fatigue life predictions, it is essential to evaluate its accuracy under quasi-static loading to observe if the damage initiated at loads below the structure's static limit are captured. The latter is important because it is these damage modes that propagate throughout the fatigue life of a structure and ultimately can lead to its final failure.

To evaluate the model, experimental results from tensile tests of single-edge notched cross-ply specimens obtained from [21] were used. The material system used by Rojas Sanchez and Waas in [21] was T800H/3631 by Toray, similar to the material system used by Davidson and Hasanyan in [45], therefore the matrix properties characterized from their experimental data in section 3.2.1 of this chapter was used. The orthotropic properties of the fiber for the NCYL and the CCM models were obtained from [47]. The specimens were of the same stacking sequence and geometry used for training the neural network in section 3.2.2. The 2 criteria used to assess the accuracy of the model were the global force-strain curve up to failure produced by the specimen and the crack density observed in the outer 90^{o} plies of the specimen. A summary of the comparison is presented in Figure 38. A close correlation between the stiffness of the force-strain curve and the load to failure are observed. To observe crack formation experimentally, Digital Image Correlation (DIC) was used in [21]. The horizontal lines of high strain concentration in the experimental results indicate the formation of a crack. Only a representative specimen of the 4 tested in [21] is shown. From the model

results, the cracks formed were identified and illustrated separately in a diagram for clarity. Results in both cases are shown at 3 points corresponding to 0.4, 0.6, and 0.8% global strain, indicated by the labels A, B, and C respectively. In the 3 cases, a similar crack density can be observed. The close correlation between the experimental and the model results demonstrates the potential of the proposed modeling method. Currently, a similar comparison is being made for a fatigue loading scenario.

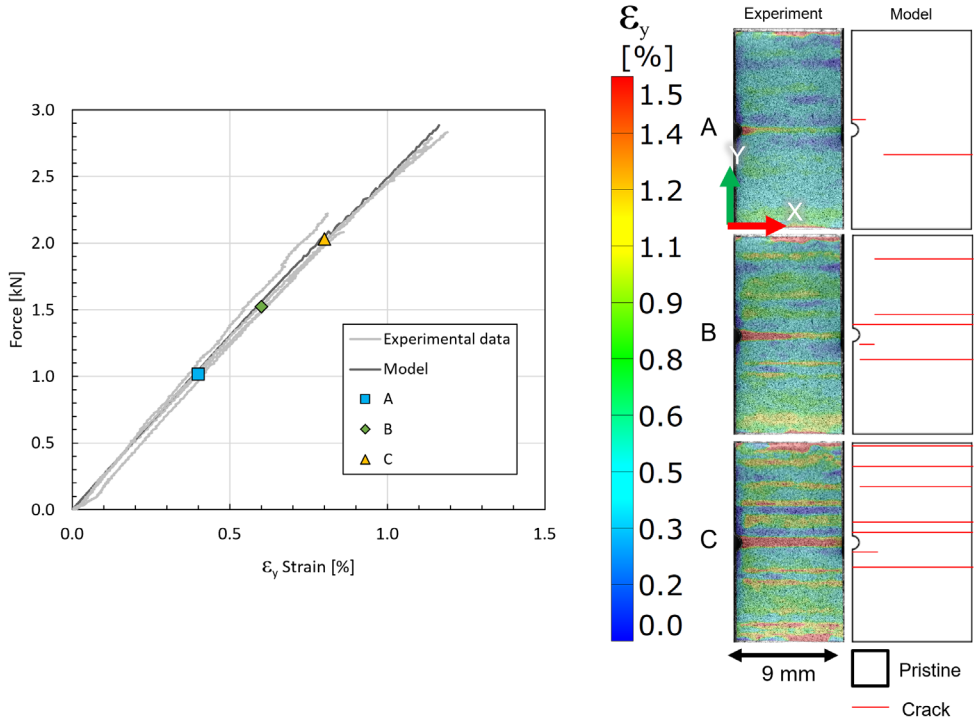

Figure 38 Comparison between single-edge notched experiment and model

4.4 Conclusions and future steps

In this chapter, a novel multiscale modeling technique for fatigue life predictions of unidirectional laminated polymer matrix composites was introduced. The model leverages multiscale analytical tools that have been developed and proven before such as NCYL and CCM, as well as FE meshing strategies like SD2M, and combines them in an efficient way to produce accurate and fast results. To accelerate the multiscale calculations required by NCYL, a neural network was trained leading to significant time reductions. The method proposed is still under development. Currently it has only been evaluated against experimental results for the case of a single-edge notched cross-ply laminate. Future work includes validating the model for fatigue loading scenarios.

Acknowledgements

The authors acknowledge the University of Michigan College of Engineering for financial support and the Michigan Center for Materials Characterization for use of the instruments and staff assistance. The authors gratefully acknowledge financial support through AFOSR grant FA9550-20-1-0014.

References

[1] W. V. Paepegem and J. Degrieck, "A New Coupled Approach of Residual Stiffness and Strength for Fatigue of Fibre-reinforced Composites," International Journal of fatigue, vol. 24, no. 7, pp. 747-762, 2002.

[2] S. M. Arnold and S. Kruch, "Differential continuum damage mechanics models for creep and fatigue of unidirectional metal matrix composites.," NASA Technical Memorandum 105213, Cleveland, Ohio, 1991.

[3] J. L. Chaboche and P. M. Lesne, "A Non-Linear Continuous Fatigue Damage Model," Fatigue Fract. Engng. Mater. Struct., vol. 11, no. 1, pp. 1-7, 1988.

[4] P. Naghipour, E. J. Pineda, B. A. Bednarcyk, S. M. Arnold and A. Waas, "Fatigue analysis of notched laminates: A time-efficient macro-mechanical approach," Journal of Composite Materials, vol. 51, no. 15, pp. 1-18, 2016.

[5] M. Kaminski, F. Laurin and J. f. Maire, "Fatigue Damage Modeling of Composite Structures: the ONERA Viewpoint," Aerospace Lab, no. 9, 2015.

[6] M. Shokrieh and L. Lessard, "Progressive Fatigue Damage Modeling of Composite Materials, Part I: Modeling," Journal of Composite Materials, vol. 34, pp. 1056-1080, 2000.

[7] M. Shrokieh and L. Lessard, "Progressive Fatigue Damage Modeling of Composite Materials, Part II: Material Characterization and Model Verification," Journal of Composite Materials, vol. 34, no. 13, pp. 1081-1116, 2000.

[8] A. Faupel, I. Meshi and C. Oskay, "Reduced order multiscale model for compression kink-band failure in composites," Journal of Composite Materials, vol. 56, no. 22, pp. 3385-3400, 2022.

[9] Z. Su and C. Oskay, "Mesh size objective fatigue damage propagation in laminated composites using the multiscale discrete damage theory," Computational Mechanics, vol. 67, pp. 969-987, 2021.

[10] C. Oskay, Z. Su and B. Kapusuzoglu, "Discrete eigenseparation-based reduced order homogenization method for failure modeling of composite materials.," Computer Methods in Applied Mechanics and Engineering, vol. 359, p. 112656, 2020.

[11] H. Hochster, Y. Bernikov, I. Meshi, S. Lin, V. Ranatunga, A. M. Waas, N. N. Shemesh and R. Haj-Ali, "Refined nonlinear micromechanical models using artificial neural networks for multiscale analysis of laminated composites subject to low-velocity impact," International Journal of Solids and Structures, vol. 264, p. 112123, 2023.

[12] J. Stuckner, S. Graeber, B. Weborg, T. M. Ricks and S. M. Arnold, "Tractable Multiscale Modeling with An Embedded Microscale Surrogate," in AIAA SciTech Forum, Virtual Event, 2021.

[13] B. G. Christoff, H. Brito-Santana and R. Talreja, "Multiscale embedded models to determine effective mechanical properties of composite materials: Asymptotic Homogenization Method combined to Finite Element Method," Composites Part C: Open Access, vol. 9, p. 100303, 2022.

[14] F. Marinelli, A. P. van den Eijnden, Y. Sieffert and R. Chambon, "Modeling of granular solids with computational homogenization: Comparison with Biot's theory," Finite Elements in Analysis and Design, vol. 119, pp. 45-62, 2016.

[15] M. H. Nguyen and A. M. Waas, "A novel mode-dependent and probabilistic semi-discrete damage model for progressive failure analysis of composite laminates - Part I: Meshing strategy and mixed-mode law," Composites Part C: Open Access 3, 2020.

[16] M. H. Nguyen and A. M. Waas, "A novel mode-dependent and probabilistic semi-discrete damage model for progressive failure analysis of composite laminates - Part II: Applications to unnotched and open-hole tensile specimens," Composites Part C: Open Access 3, 2020.

[17] M. H. Nguyen and A. M. Waas, "Efficient and Validated Framework for Probabilistic Progressive Failure Analysis of Composite Laminates," AIAA Journal, pp. 1-21, 2022.

[18] R. A. Schapery, "Schapery, R. A. "A theory of mechanical behavior of elastic media with growing damage and other changes in structure," Journal of the Mechanics and Physics of Solids, vol. 38, no. 2, pp. 215-253, 1990.

[19] J. Guilleminot, C. Soize and D. Kondo, "Mesoscale probabilistic models for the elasticity tensor of fiber reinforced composites: Experimental identification and numerical aspects," Mechanics of Materials, vol. 41, no. 12, pp. 1309-1322, 2009.

[20] J. Zhang, M. Shields and S. TerMaath, "Probabilistic modeling and prediction of out-of-plane unidirectional composite lamina properties," Mechanics of Advanced Materials and Structures, vol. 28, no. 22, pp. 2310-2326, 2020.

[21] J. F. Rojas Sanchez and A. M. Waas, "High resolution imaging of fatigue damage evolution in fiber reinforced composites using digital volume correlation for model validation," in AIAA SciTech 2022 Forum, San Diego, 2022.

[22] Y. Pan, L. Lorga and A. A. Pelegri, "Analysis of 3D random chopped fiber reinforced composites using FEM and random sequential adsorption," Computational Materials Science, vol. 43, no. 3, pp. 450-461, 2008.

[23] S. A. Elnekhaily and R. Talreja, "Damage initiation in unidirectional fiber composites with different degrees of nonuniform fiber distribution," Composite Science and Technology, vol. 155, pp. 22-32, 2018.

[24] J. F. Husseini, E. J. Pineda and S. E. Stapleton, "Generation of artificial 2-D fiber reinforced composite microstructures with statistically equivalent features," Composites Part A, vol. 164, 2023.

[25] J. Aboudi, S. M. Arnold and B. A. Bednarcyk, Micromechanics of composite materials, Waltham: Elsevier, 2013.

[26] N. Takeda and S. Ogihara, "Micromechanical characterization of local deformation in interlaminar-toughened CFRP laminates," Composites Part A: Applied Science and Manufacturing, vol. 29, no. 12, pp. 1545-1552, 1998.

[27] Z. Hashin and B. W. Rosen, "The elastic moduli of fiber-reinforced materials," Journal of applied mechanics, vol. 31, no. 2, pp. 223-232, 1964.

[28] M. Mehdikhani, M. Aravand, B. Sabuncuoglu, M. G. Callens, S. V. Lomov and L. Gorbatikh, "Full-field strain measurements at the micro-scale in fiber-reinforced composites using digital image correlation," Composite Structures, vol. 140, pp. 192-201, 2016.

[29] F. Aymerich, A. Dalla Via and M. Quaresimin, "Energy absorption capability of nanomodified glass/epoxy laminates," Procedia Engineering, vol. 10, pp. 780-785, 2011.

[30] L. Li, S. V. Lomov and X. Yan, "Correlation of acoustic emission with optically observed damage in a glass/epoxy woven laminate under tensile loading," Composite Structures, vol. 123, pp. 45-53, 2015.

[31] A. Todoroki, Y. Tanaka and Y. Shimamura, "Luminance change method for strain and matrix cracking monitoring of glass/epoxy composites with EL backlight," Composites Science and Technology, vol. 63, no. 2, pp. 273-281, 2003.

[32] D. P. Jansen, D. A. Hutchins and J. T. Mottram, "Lamb wave tomography of advanced composite laminates containing damage," Ultrasonics, vol. 32, no. 2, pp. 83-89, 1994.

[33] K. R. Leonard, E. V. Malyarenko and M. K. Hinders, "Ultrasonic Lamb wave tomography," Inverse Problems, vol. 18, pp. 1795-1808, 2002.

[34] S. M. Prasad, K. Balasubramaniam and C. V. Krishnamurthy, "Structural health monitoring of composite structures using Lamb wave tomography," Smart Materials and Structures, vol. 13, pp. N73-N79, 2004.

[35] E. Jo, S. Lee, C. Hong and W. Ji, "In situ observation of interactive failure modes in a single-edge notched symmetric cross-ply laminate using synchrotron X-ray tomography," Composites Part A, vol. 128, 2019.

[36] C. Hong and W. Ji, "Complementary ex situ investigations of various fracture modes in a single-edge-notched symmetric cross-ply laminate subjected to tensile loading," Composites Communications, vol. 17, pp. 28-31, 2020.

[37] A. Buljac, C. Jailin, A. Mendoza, J. Neggers, T. Tailandier-Thomas, A. Bouterf, B. Smaniotto and F. Hild, "Digital Volume Correlation: Review of Progress and Challenges," Experimental mechanics, vol. 58, pp. 661-708, 2018.

[38] S. Lee, E. Jo and W. Ji, "Digital volume correlation technique for characterizing subsurface deformation behavior of a laminated composite," Composites Part B: Engineering, vol. 194, 2020.

[39] S. Ferraro and S. Pellegrino, "Size effects in plain-weave Astroquartz deployable thin shells," Journal of Composite Materials, vol. 55, no. 18, pp. 2417-2430, 2021.

[40] M. Mehdikhani, C. Breite, Y. Swolfs, J. Soete, M. Wevers, S. V. Lomov and L. Gorbatikh, "Digital volume correlation for meso/micro in-situ damage analysis in carbon fiber reinforced composites," Composites Science and Technology, vol. 213, 2021.

[41] E. Bar-Kochba, J. Toyjanova, E. Andrews, K. S. Kim and C. Franck, "A Fast Iterative Digital Volume Correlation Algorithm for Large Deformations," Experimental Mechanics, vol. 55, pp. 261-274, 2015.

[42] N. Takeda and S. Ogihara, "Micromechanical characterization of local deformation in interlaminar-toughened CFRP laminates," Composites Part A: Applied Science and Manufacturing, vol. 29, no. 12, pp. 1545-1552, 1998.

[43] P. A. Carraro and M. Quaresimin, "A stiffness degradation model for cracked multidirectional laminates with cracks in multiple layers," International Journal of Solids and Structures, vol. 58, pp. 34-51, 2015.

[44] D. Zhang and A. M. Waas, "A micromechanics based multiscale model for nonlinear composites," Acta Mechanica, vol. 225, no. 4-5, pp. 1391-1417, 2014.

[45] P. Davidson, A. Hasanyan and A. M. Waas, "Multiscale fatigue modeling of composites," American Institute of Aeronautics and Astronautics, 2018.

[46] J. C. Hashin and B. W. Rosen, "The elastic moduli of fiber reinforced materials," J. Appl. Mech., vol. 31, pp. 223-228, 1964.

[47] F. Rojas-Sanchez and A. M. Waas, "Microscale experimental results and their implications for mesoscale modeling of damage initiation in cross-ply fiber reinforced composites," Composites Part B: Engineering, vol. 257, 2023.